nature chemical engineering

Article

https://doi.org/10.1038/s44286-024-00090-w

Connected three-dimensional polyhedral frames for programmable liquid processing

Received: 10 November 2023

Accepted: 31 May 2024

Yiyuan Zhang[1], **Zhandong Huang**[2]✉, **Feifei Qin**[3,4], **Hongzhou Wang**[5], **Kai Cui**[2], **Kun Guo**[2], **Zheren Cai**[6], **Xiaobing Cai**[7], **Junfeng Xiao**[8], **Jan Carmeliet**[4], **Jinjia Wei**[2], **Yanlin Song**[6], **Jun Yang**[8]✉ & **Liqiu Wang**[1]✉

Human civilization relies heavily on the ability to precisely process liquids. Switching between liquid capture and release plays a fundamental role in the handling of various liquids, with applications that demand reversible, spatially and temporally precise, volumetrically accurate and programmable control over the liquid, independent of the details of the employed solid tools and processed liquids. However, current fluidic techniques do not fully meet these requirements. Here we present connected polyhedral frames to effectively address this challenge by tailoring liquid continuity between frames to dictate the liquid capture or release of individual frames, with an overall network that is readily switchable locally, dynamically and reversibly. Each frame captures or releases liquids, independent of its base materials, structures and processed liquids. The connected polyhedral frames are a versatile tool that enables many important functions including three-dimensional (3D) programmable patterning of liquids, 3D spatiotemporal control of concentrations of multiple materials, packaging of 3D liquid arrays and large-scale manipulation of multiple liquids, thus considerably advancing many fields, including interface science and soft materials.

Many research, industrial and medical applications rely on the ability to precisely capture and release various chemical and biological fluids[1–7]. Fluids have no fixed shape, making them difficult to control with conventional tools[3,7]. They can readily wet solids, leaving residues that foul tools and causing liquid loss and intersample contaminations, and contribute to the global problem of plastic waste as disposable pipettes and microtubes are widely used to handle the fluids[8,9]. A long-standing challenge is to design a platform that enables the switchable capture and release of liquids with precise spatial and temporal control and accurate volumes of the fluid. We address this challenge with connected polyhedral frames (CPFs) where each frame functions to programmably capture or release liquid depending solely on the liquid continuity with its below neighbor. This continuity can be readily switched locally, dynamically and reversibly with many available tools: a double-rod connection between frames, droplet-to-droplet connection and liquid film connection to facilitate liquid continuity, for example, and liquid film rupture, interfacial gelation and interfacial polymerization to disrupt liquid continuity. The CPFs thus form a fluidic tool for versatile, programmable and three-dimensional

---

[1] Department of Mechanical Engineering, The Hong Kong Polytechnic University, Hong Kong, China. [2] School of Chemical Engineering and Technology, Xi'an Jiaotong University, Xi'an, China. [3] Institute of Extreme Mechanics, Northwestern Polytechnical University, Xi'an, China. [4] Chair of Building Physics, Department of Mechanical and Process Engineering, ETH Zürich (Swiss Federal Institute of Technology in Zürich), Zurich, Switzerland. [5] Jiangxi Institute of Mechanical Science, Nanchang, China. [6] Key Laboratory of Green Printing, Institute of Chemistry, Chinese Academy of Sciences (ICCAS), Beijing Engineering Research Center of Nanomaterials for Green Printing Technology, Beijing National Laboratory for Molecular Sciences (BNLMS), Beijing, China. [7] State Key Laboratory for Strength and Vibration of Mechanical Structures, School of Aerospace Engineering, Xi'an Jiaotong University, Xi'an, China. [8] Shenzhen Institute for Advanced Study, University of Electronic Science and Technology of China, Shenzhen, China.
✉e-mail: huangzhandong@xjtu.edu.cn; junyang@uestc.edu.cn; liqiu.wang@polyu.edu.hk

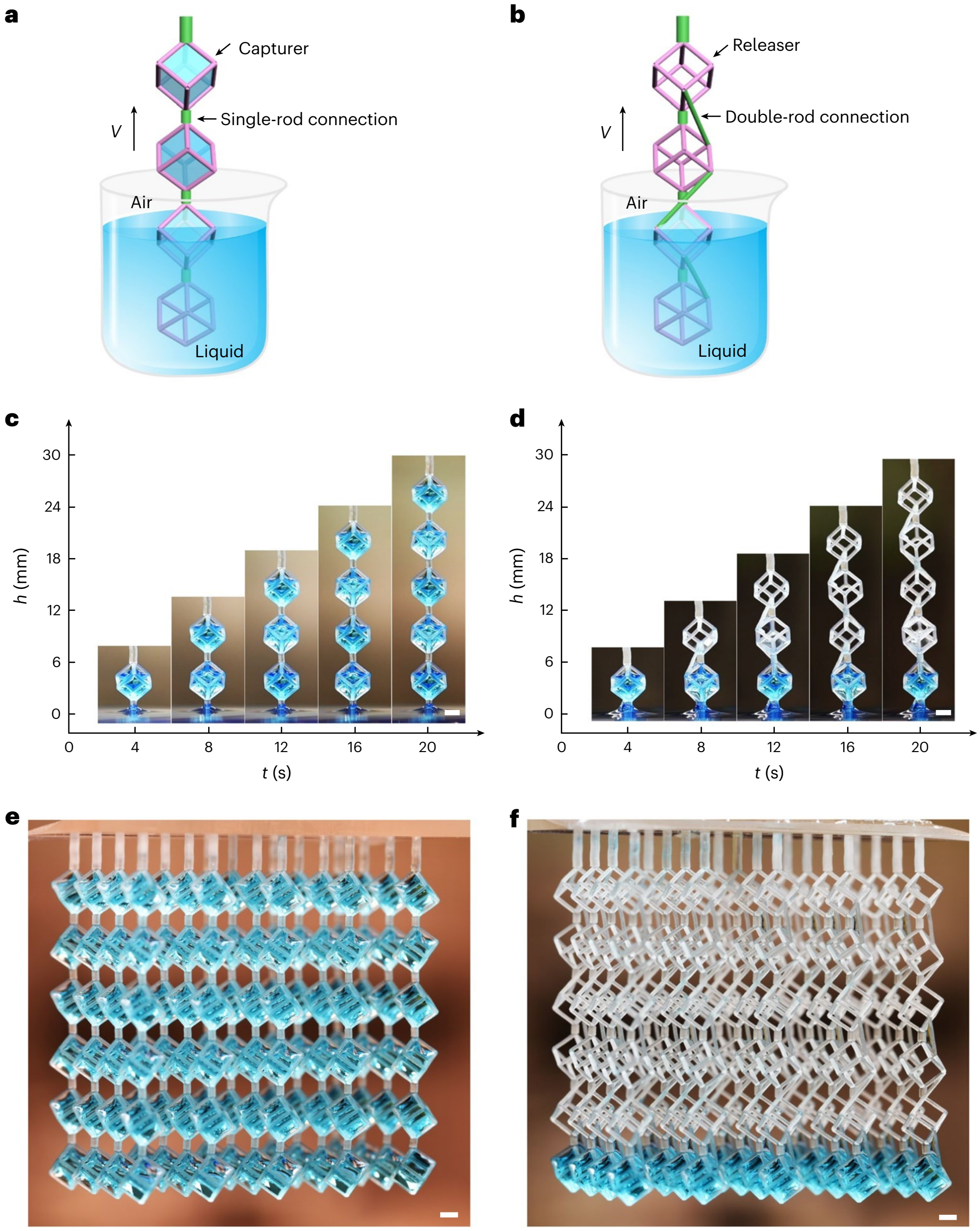

Fig. 1 | The CPFs. a,**b**, Schematic diagram of the CPFs. When the CPFs are slowly lifted out of the liquid, the single-rod-connected capturers capture and retain liquid (**a**), while double-rod-connected releasers release their imbibed liquid (**b**). **c**, Liquid can be captured and retained as the capturers are lifted from the liquid. **d**, The releasers release their liquid when they are lifted from the liquid. **e**, The 3D liquid array is prepared using a capturer array. **f**, The 3D releaser array still releases the liquid. The liquid in **c**–**f** is blue-dyed water. Scale bars, 2 mm.

(3D) processing of liquids, demonstrated with patterning of unary and binary liquids, multimaterial manufacturing, reversible sampling and release, effective bacterial encapsulation, high-flow evaporative humidifiers and efficient CO_2 capture. To highlight the applicability, practical utility and some key advantages of CPFs, we summarize the limitations of existing fluidic techniques, unique features of CPFs and eight applications that demonstrate advantages of the CPFs over the existing fluidic technologies in Supplementary Table 1.

Results

CPF design

The CPFs are wettable to the processed liquid (Fig. 1a,b). When the frames are slowly lifted out of the liquid, the capillary force can overcome gravity if the frame size is within the capillary length of the processed liquid, enabling the frames to capture the liquid. Interesting phenomena emerge when the frames are connected in different ways. Taking water as an example, when lifting the CPFs from water, single-rod connected frames capture and retain water (Fig. 1c and Supplementary Video 1); however, water drains from double-rod connected frames (Fig. 1d and Supplementary Video 1). Therefore, frames above the single-rod connection function as a capturer (the frame unit that captures and retains liquids), while the frames above the double-rod connection serve as a releaser (the frame unit imbibes but releases liquids). This phenomenon can be extended to a 3D array of CPFs (Fig. 1e,f and Supplementary Video 1). The last row of frames in Fig. 1f serves as the capturers; the captured liquid can be completely released by adding double-rod structures as shown in Supplementary Fig. 1. Furthermore, the steerable liquids can be extended from aqueous solutions to biologically relevant fluids, hydrogels, organic solvents, polymer solutions and silicone oils by designing the size of the polyhedral frame

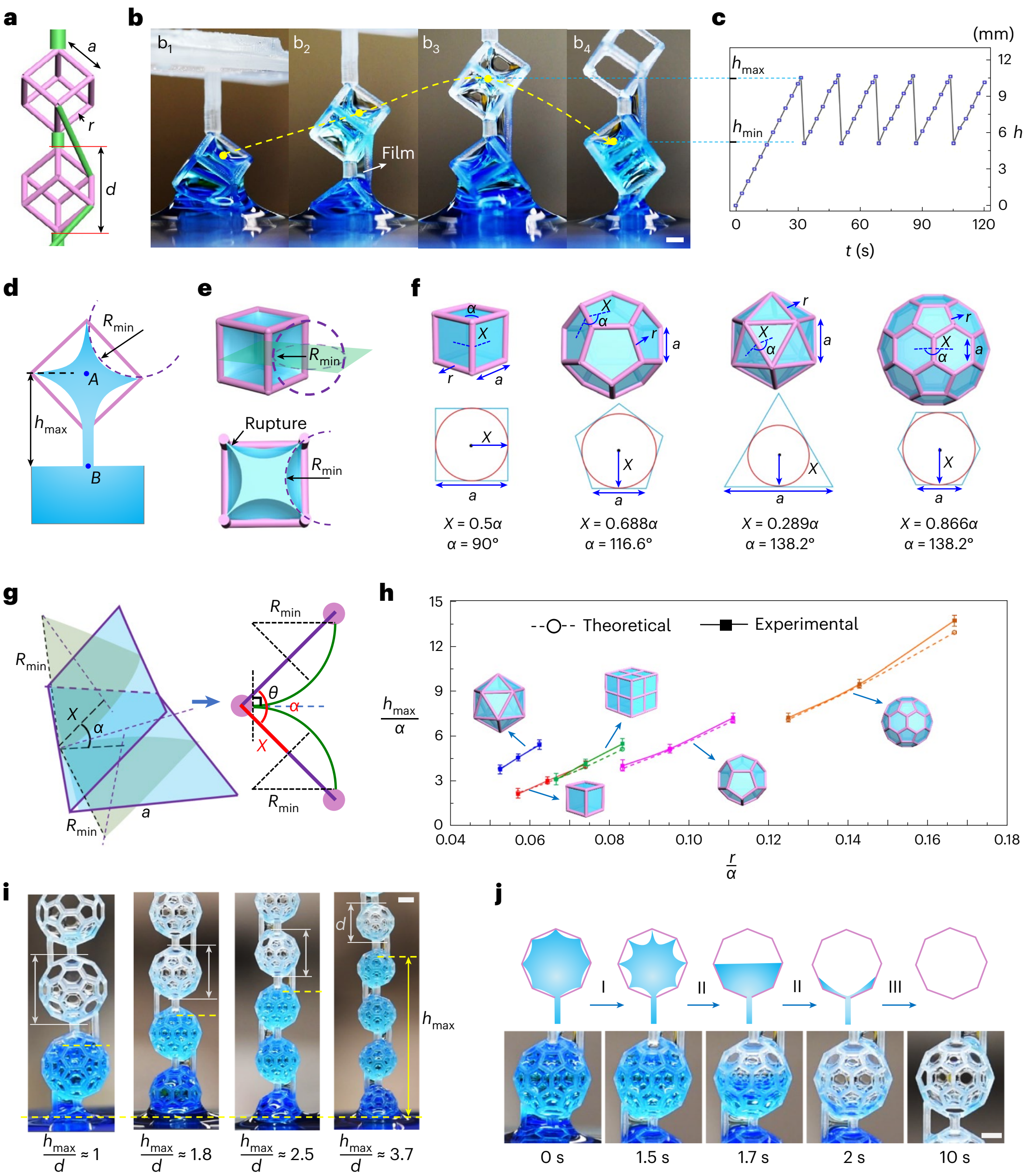

Fig. 2 | The working mechanism of liquid capture–release by CPFs. **a**, Structural diagram of the releaser. *a* and *r* are the side length and rod radius of the PFs, respectively, and *d* is the diameter of the circumscribed sphere of the PFs. **b**, The release process of releasers. During this process, a liquid film is formed between the double-rod connection. Scale bar, 1 mm. **c**, When the releasers are slowly lifted from the liquid, the liquid height (*h*) in the CPFs varies periodically with time between a maximum (h_{max}) and minimum (h_{min}). **d**, The *h* reaches its maximum when the curvature radius of the rising meniscus in the frame becomes minimum (R_{min}). **e**, Three-dimensional schematic diagram of R_{min} and the critical state of liquid rupture when two adjacent menisci with R_{min} contact. **f**,**g**, The key factors that affect the value of R_{min} for releasers with different geometries include the radius of the inscribed circle of the polygonal faces (*X*), the dihedral angle of the polyhedral frame (*α*), the contact angle of liquid on the frame surface (*θ*), the polyhedral side length (*a*) and the frame rod radius (*r*). **h**, Experimentally measured and theoretically calculated $\frac{h_{max}}{a}$ of releasers with different geometry and size parameter $\frac{r}{a}$ (data are presented as mean ± s.d. of *n* = 3 replicates). **i**, By adjusting the ratio of h_{max} over *d*, the number of liquid-filled PFs above the bulk liquid can be controlled. **j**, Three stages of the release process, the height-dominated release (stage I), free fall release (stage II) and film release (stage III). The water is dyed blue to facilitate visualization. In **i** and **j**, the scale bars are 2 mm.

(PF) within the capillary length of the corresponding liquid (Extended Data Fig. 1 and Supplementary Fig. 2). CPFs printed with other materials, including stainless steel, biocompatible polylactic acid (PLA) and polyurethane (PU), all showed the capture and release of corresponding liquids (Supplementary Fig. 3). These findings show the versatility of CPFs to different liquids and frame materials.

CPF capture and release mechanisms

Understanding the mechanism of liquid capture by the CPFs is straightforward: when they are lifted from the liquid, the liquid-philic frames provide a capillary driving force to capture the liquid, while the single rod between the frames acts only as a mechanical connection without providing a pathway for liquid drainage between frames[10]. Understanding their mode of liquid release, however, requires experiments, numerical simulations and analysis. Taking the cubic PF as an example (Fig. 2a), we analyze the release process in detail (Fig. 2b and Supplementary Video 2). When the CPFs are slowly lifted from the liquid, a liquid film forms between the double-rod connection and, thus, connects the liquid in the frame with the bulk liquid below. Thereafter, when the liquid in the frame rises to a critical height, gravity-dominated liquid drainage occurs in the frame. We tracked the evolution of liquid height (h), shown as h–t (height–time) curves in Fig. 2c. Figure 2c indicates that h varies periodically with t between a maximum (h_{max}) and a minimum height (h_{min}).

To understand the liquid-height changes in rising CPFs, an analogy can be drawn to a tube with a nonuniform cross-section (Supplementary Discussion 1). As shown through numerical simulations of capillary rise in uniform and nonuniform capillary tubes (Supplementary Video 3), when a nonuniform tube is slowly lifted from the liquid, the height h of the capillary rise first gradually increases to its maximum h_{max} and then suddenly decreases; h_{max} appears where the curvature radius R of the rising meniscus reaches its minimum[11]. This simulation corresponds to one cycle of the periodic changes of liquid height (h) in the CPFs. Therefore, as the CPFs are pulled out of the liquid (Fig. 2b$_1$,b$_2$), a liquid film forms between the double-rod connection and, thus, connects the liquid in the frame with the bulk liquid below. The pressure difference ($P_{\mathrm{B}} - P_{\mathrm{A}}$ in Fig. 2d, with P_{B} and P_{A} being the pressure at points B and A, respectively) is generated by the rising liquid in the frame and equals ρgh. As h increases, the liquid in the frame shrinks inward, decreasing R in supporting the greater liquid weight. Meanwhile, the decrease in liquid volume shows the release (Fig. 2b$_2$,b$_3$). When the liquid shrinks to its critical state, the state at which the adjacent menisci contact, the curvature radius R of the corresponding meniscus reaches its minimum R_{min} (Fig. 2d,e) and the liquid height h reaches its maximum h_{max} (Fig. 2b$_3$). Subsequently, the liquid ruptures in the frame, h returns to h_{min} (Fig. 2b$_4$) and the process repeats in the next frame. The lifting process of the CPFs from water into air was simulated by a pseudo-potential two-phase lattice Boltzmann model. Extended Data Fig. 2 shows the simulated liquid-pressure changes in the CPFs during the frame rising process (Supplementary Video 4), further confirming the working mechanism of the CPFs that serve as the capturer and the releaser, respectively.

By analyzing the static equilibrium at the critical state (Fig. 2d,e), h_{max} can be readily obtained. At this state, the liquid pressure at point A (P_{A}; Fig. 2d) is $P_{\mathrm{B}} - \rho gh_{\mathrm{max}}$ from hydrostatic analysis and $P_{\mathrm{a}} - 2\sigma/R_{\mathrm{min}}$ from the application of the Laplace equation to the meniscus. Here, ρ, σ and g are the liquid density, surface tension and gravitational acceleration, respectively. P_{a} is the ambient air pressure (a constant), and P_{B} is the liquid pressure at Point B (Fig. 2d) that equals P_{a}. Therefore,

$$h_{\mathrm{max}} = \frac{2\sigma}{\rho g R_{\mathrm{min}}}, \tag{1}$$

which indicates that, for a given liquid, h_{max} is mainly determined by R_{min} and is independent of the connecting rod's parameters. This is experimentally verified: specifically, h_{max} keeps constant when changing the length of the connecting rod, and different ways of double-rod connection induce only a small difference in h_{max} (Supplementary Fig. 4).

The theoretical general expression of R_{min} reads as follows for releasers with different geometries and size parameters (Supplementary Discussion 2):

$$R_{\mathrm{min}} = \frac{X}{\sin\frac{\alpha}{2}} + r\cos\theta\cot^2\frac{\alpha}{2} - \sqrt{r^2\cot^4\frac{\alpha}{2}(\cos^2\theta + 1) + \frac{2rX\cos\theta}{\sin\frac{\alpha}{2}}\cot^2\frac{\alpha}{2}}, \tag{2}$$

where X is the radius of the inscribed circle of the polygonal faces of diverse PFs as shown in Fig. 2f, α is the dihedral angle of the polyhedral frame and θ is the contact angle of the frame surface with the liquid. a and r are the polyhedral side length and frame rod radius, respectively. The general expression of R_{min} is derived from the geometric relationship between the liquid film and the frame at the critical state when the adjacent meniscus of the minimum curvature radius of the releaser contacts on the bisector of the corresponding polyhedral dihedral angle (Fig. 2g). The detailed derivation and analysis process is included in Supplementary Discussion 2. Nondimensionalizing R_{min} with a yields

$$\frac{R_{\mathrm{min}}}{a} = \frac{C_1}{\sin\frac{\alpha}{2}} + \frac{r}{a}\cos\theta\cot^2\frac{\alpha}{2} - \sqrt{\left(\frac{r}{a}\right)^2\cot^4\frac{\alpha}{2}(\cos^2\theta + 1) + \frac{r}{a}\cos\theta\frac{2C_1\cot^2\frac{\alpha}{2}}{\sin\frac{\alpha}{2}}}, \tag{3}$$

where C_1 is a constant determined by the geometry of the releaser which is defined by $X = C_1 a$ (the fixed relationship between X and side length a), and their values are listed in Fig. 2f. The specific dimensionless expressions of R_{min} are derived and summarized in Supplementary Discussion 2 for releasers with different geometries by substituting the values of the geometric parameters C_1 and α into equation (3).

Substituting equation (3) into equation (1) yields

$$\begin{aligned}\frac{h_{\mathrm{max}}}{a} &= \frac{2\sigma}{\rho g\frac{R_{\mathrm{min}}}{a}} \times \frac{1}{a^2}\\ &= \frac{2\sigma}{\rho g\left[\frac{C_1}{\sin\frac{\alpha}{2}} + \frac{r}{a}\cos\theta\cot^2\frac{\alpha}{2} - \sqrt{\left(\frac{r}{a}\right)^2\cot^4\frac{\alpha}{2}(\cos^2\theta+1) + \frac{r}{a}\cos\theta\frac{2C_1\cot^2\frac{\alpha}{2}}{\sin\frac{\alpha}{2}}}\right]} \times \frac{1}{a^2}.\end{aligned} \tag{4}$$

To verify the validity of equation (4), we compared the theoretically calculated and experimentally measured $\frac{h_{\mathrm{max}}}{a} - \frac{r}{a}$ curves for releasers with different geometries. In the experiment (Extended Data Fig. 3), the contact angle of water on the solid surface of the releasers is 65°, so θ is taken as 65° for the theoretical calculations. As shown in Fig. 2h, the experimental results are in good agreement with the theoretical calculations, supporting that h_{max} can be controlled by designing the frame's shape and size. By adjusting the ratio of h_{max} over d (the diameter of the circumscribed sphere of the polyhed ral frame), the number of liquid-filled frame units above the bulk liquid can be programmed as shown in Fig. 2i, and $h_{\mathrm{max}} < d$ is the condition for no liquid capture.

Based on equation (3), we can isolate the effect of the contact angle θ and size parameter $\frac{r}{a}$ on $\frac{R_{\mathrm{min}}}{a}$. The typical $\frac{R_{\mathrm{min}}}{a} - \cos\theta$ curves and the $\frac{R_{\mathrm{min}}}{a} - \frac{r}{a}$ curves are included in Supplementary Discussion 2, showing that $\frac{R_{\mathrm{min}}}{a}$ increases with the increase of θ, which is associated with the decrease of the frame liquid-philicity, and $\frac{R_{\mathrm{min}}}{a}$ decreases with the increase of $\frac{r}{a}$ owing to the increase in solid surface area and capillarity. Both the $\frac{R_{\mathrm{min}}}{a} - \cos\theta$ and the $\frac{R_{\mathrm{min}}}{a} - \frac{r}{a}$ curves shed light on how the geometry of the releaser affects its $\frac{R_{\mathrm{min}}}{a}$: under the same contact angle θ and size parameter $\frac{r}{a}$, the releaser with the icosahedron geometry provides the minimum $\frac{R_{\mathrm{min}}}{a}$, followed by the cube and dodecahedron; the releaser with geometry of the truncated icosahedron has the maximum $\frac{R_{\mathrm{min}}}{a}$. Using numerical simulation and experiments, we corroborate the effect of the frame surface wettability on h_{max} (Extended Data Fig. 4). Both show that h_{max} gradually decreases with an increase in contact angle (~5–85°).

Next, we studied the release process in the frame that consists of three stages (Fig. 2j and Supplementary Discussion 3). Stage I starts from the beginning and ends at $h = h_{\mathrm{max}}$, the liquid in the frame gradually shrinks inward and drains downward. The releasing volume flow rate at this stage (Q_{I}) is defined as $Q_{\mathrm{I}} = -F'(h)\frac{\mathrm{d}h}{\mathrm{d}t}$, where $F(h)$ is the function of liquid volume at different heights in the frame. Because this release stage is mainly governed by the rising height, it is called the 'height-dominated release'. Stage II refers to the moment when the liquid ruptures and falls rapidly (<0.6 s). After the liquid ruptures, the meniscus in the frame flattens instantly, making the Laplace pressure difference across the meniscus close to zero. Without the support of the Laplace pressure difference, the liquid falls almost in a free fall[12]. Therefore, stage II is named 'free-fall release', and the releasing volume flow rate (Q_{II}) is given as $Q_{\mathrm{II}} = \sqrt{\frac{g}{2h_{\mathrm{max}}}}F(h_{\mathrm{max}})$. Experiments have confirmed that release stages I and II can release most of the liquid in the frame, but their release proportions vary in frames with different geometries (Supplementary Video 5). For example, stage I occupies a larger release proportion in cubic and pentahedral frames (Fig. 2b and Supplementary Fig. 5), while stage II contributes more to icosahedral and truncated icosahedral frames (Supplementary Fig. 5). Stage III is the final release process until the liquid film between the double-rod connection ruptures. At this stage, the remaining liquid releases through the liquid film, which is a viscous flow process driven by the pressure gradient in the film[13,14]. Hence, stage III is named the 'film release' stage.

Switching between capture and release

The release mechanism shows that the liquid continuity constructed by the liquid film between the double-rod connection is the key to triggering liquid drainage, which inspired us to achieve switching between liquid capture and release by establishing or breaking this liquid continuity. Destroying the liquid continuity can switch release into capture; conversely, the establishment of liquid continuity will convert capture into release (Supplementary Fig. 6a). We demonstrated two approaches to breaking the liquid continuity by destroying the liquid film between the double-rod connection, that is, directly piercing the liquid film with a swab or imposing a very small lifting speed to promote spontaneous liquid film rupture induced by evaporation (Supplementary Video 6). Likewise, two simple methods for establishing liquid continuity are provided. One way is to create droplet-to-droplet contact, which can release the captured liquid (Supplementary Video 6). Alternatively, a soap film is used to connect the dispersed liquids in the capturers, which also releases the captured liquid (Supplementary Video 6). To completely release the liquid, the size of the soap film needs to meet the condition as illustrated in Supplementary Fig. 6b; when a soap film with longitudinal length L contacts the capturer, the distance from the contact point to the bottom of the film (L_1) should be larger than h_{max} (Supplementary Video 7). Following this principle, soap films with predesigned patterns are applied to release liquids at designated locations to obtain designed liquid patterns (Supplementary Fig. 6c and Supplementary Video 7). In addition, the liquid in the capturer array can be fully released by the soap film array (Supplementary Fig. 6d and Supplementary Video 7), which renders a facile and efficient method for recovering liquids from CPFs. The function (liquid capture or release) of each CPF is readily switched back after being switched as well simply by triggering the 'liquid continuity change', a feature termed as 'reversible' (Supplementary Table 1c). The capability to reversibly capture and release liquids will potentially benefit many applications including biological sampling, medical diagnostics and chemical synthesis.

Programmable 3D liquid patterning and applications

Programmable 3D patterning of liquids is of importance for the 3D spatiotemporal control of biological and chemical processes[15,16] but still remains challenging with current fluidic devices. Here, we overcome this limitation with switchable capturing and releasing CPFs, achieving programmable 3D patterning of liquids. The basic coding principle of the programmable liquid patterning is shown in Fig. 3a,b, that is, releasers above the double-rod connection are denoted as '0', and capturers above the single-rod connection are denoted as '1'. By designing the frame connections, the 3D spatial arrangement of capturers and releasers can be programmed to acquire the desired liquid patterns (Supplementary Video 8). To prepare the two-dimensional (2D) liquid pattern, the pattern is first disassembled into digital codes of '1' and '0' pixel by pixel, that is, pixels in the target pattern area are coded as '1' and pixels in the blank background area are coded as '0'. Based on the digital codes, we can deduce the spatial arrangement of single-rod and double-rod connections between the frames, and the expected liquid pattern can be obtained after printing the predesigned model. Two-dimensional letter patterns of 'U', 'W' and 'O' are successfully produced using preprogrammed CPFs (Fig. 3c and Supplementary Video 8), as an example. This principle can readily be exploited to achieve 3D liquid patterning by first disassembling 3D patterns into 2D patterns layer by layer. Building on this concept, we prepared hourglass-like and other predesigned 3D liquid patterns as exhibited in Fig. 3d and Fig. 3e, respectively (Supplementary Video 8).

Compared with 3D unary liquid patterning, 3D patterning of binary liquids can open broader applications because it allows 3D parallel multivariate functions. Combined with interfacial reactions, here we accomplished programmable 3D patterning of binary liquids using the switchable capturing and releasing of CPFs. The detailed patterning principle is elucidated in Fig. 3f. The CPFs first capture liquid A and then encapsulate it through interfacial solidification (for example, polymerization or gelation). Subsequently, these solidified liquid interfaces will break the liquid continuity and block the release process of the adjacent releasers, converting the releasers into capturers to capture liquid B, finally forming the 3D patterns of binary liquids. Employing interfacial gelation, we elaborate the 3D patterning of water, hydrogel and drug-containing aqueous solutions. The 3D pattern of gellan gum solution and water is illustrated in Fig. 3g. By designing alternately adjacent single-rod and double-rod connections, 3D alternately distributed capturers and releasers were obtained. After capturing red-dyed gellan gum solution and blue-dyed water in sequence, a 3D binary liquid pattern with alternating red and blue pixels was prepared. The 3D pattern of two gellan gum solutions is exhibited in Supplementary Fig. 7. By designing layer-by-layer alternating single-rod and double-rod connections, 3D layer-by-layer alternating capturers and releasers were generated. After capturing red- and green-dyed gellan gum solutions in sequence, a 3D binary liquid pattern with alternating red and green layers was created. The liquid-patterning processes in Fig. 3g and Supplementary Fig. 7 both take advantage of the gelling properties of gellan gum at low temperatures (Supplementary Video 9). Because a wide range of biomaterials and chemicals can be incorporated into aqueous solutions and hydrogels, their 3D patterns of binary liquids can be used for multipart cell or bacterial culture[17,18], 3D chemical-gradient generation[16,19] and multimaterial structure fabrication[20] in cell–cell communication[21], bacterial ecology[22], chemical engineering[23] and hybrid bioprinting.

To demonstrate the practical utility of 3D patterning of binary liquids, we show its application in 3D spatiotemporal control of multimaterial concentration distributions through numerical simulations and experiments. The simulated 3D spatial concentration distribution of the two substances is shown in Extended Data Fig. 5 in their different binary liquid patterns during diffusion in water. By tuning the diffusion coefficient and designing diverse binary liquid patterns, the 3D concentration distribution of these two substances can be spatiotemporally controlled. We validated this by realizing controlled multidrug release using the interfacial gelation of $CaCl_2$ in sodium alginate. Vitamins B_2 and B_{12} were chosen to represent the two different drugs because of the high color contrast of their aqueous solutions. Their 3D binary liquid pattern is displayed in Fig. 3h, where the red vitamin B_{12} solution is encapsulated in the truncated icosahedron frame and the yellow vitamin B_2 solution is encapsulated in cubic frames. The specific patterning process is recorded in Supplementary Fig. 8. The capturers first capture the $CaCl_2$ solution dissolved with vitamin B_{12} and complete the liquid encapsulation in sodium alginate. Then the release-blocked releasers capture the viscous gellan gum solution dissolved with vitamin B_2. Their release process in water and the corresponding release profiles are presented in Fig. 3i and Fig. 3j, respectively, implying that vitamin B_2 in gellan gum solution is rapidly released, while the encapsulated vitamin B_{12} shows slow release due to the membrane barrier. The thickness of the membrane can be flexibly adjusted by changing the interfacial gelation time, thereby controlling the release rate ratio of the two different drugs. By designing the spatial arrangement of capturers and releasers, the spatial concentration distribution of the two drugs can be further manipulated. Therefore, 3D spatial and temporal control of multidrug release can be successfully achieved.

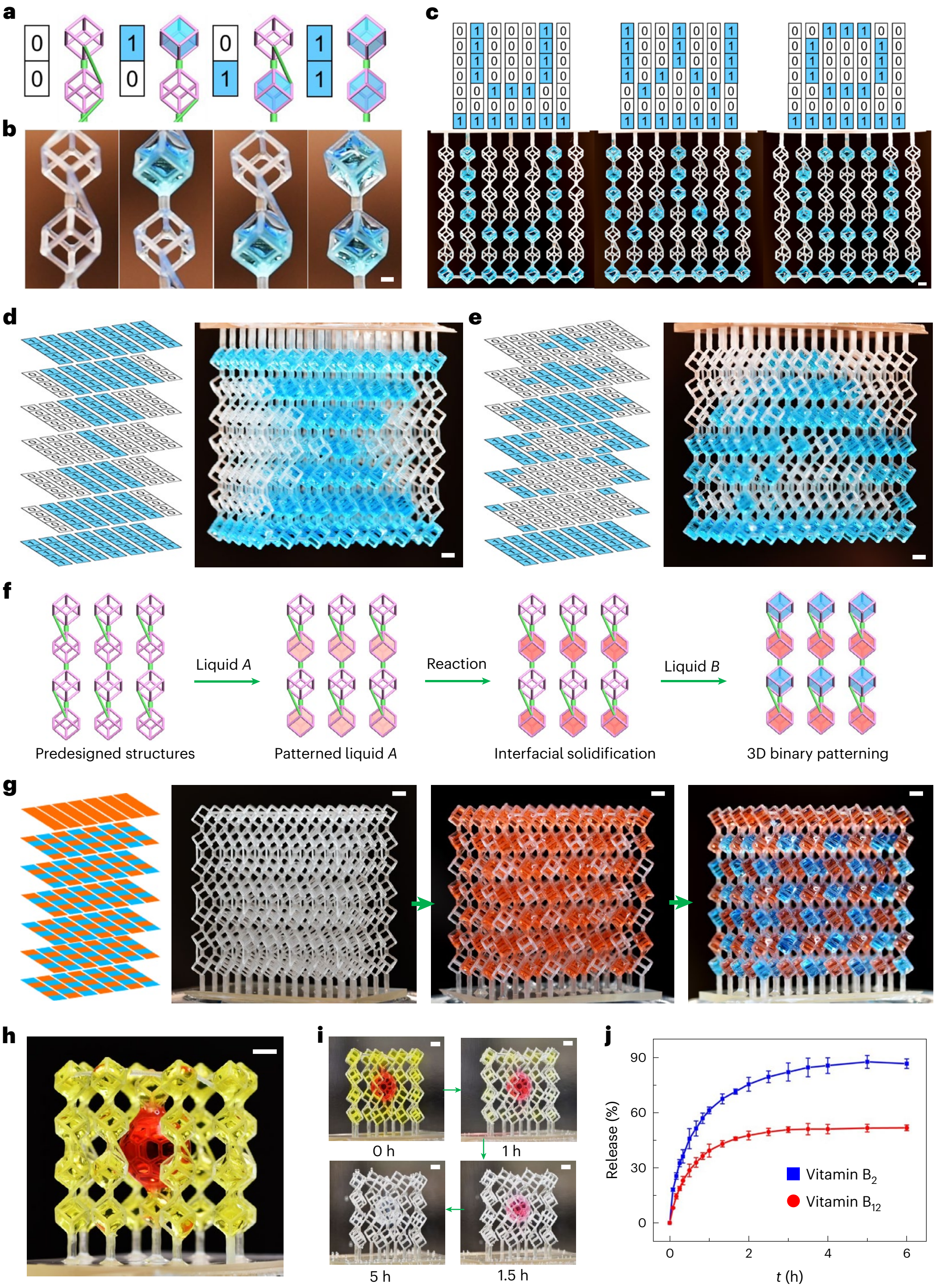

Fig. 3 | Programmable 3D liquid patterning. a, Coding principle for programmable 3D liquid patterning: releasers above the double-rod connection are denoted as '0', and capturers above the single-rod connection are denoted as '1'. **b**, The corresponding liquid patterns obtained based on the coding principle. Scale bar, 1 mm. **c**, Two-dimensional letter patterns of 'U', 'W' and 'O' created using preprogrammed CPFs. **d**,**e**, The hourglass-like (**d**) and other predesigned (**e**) 3D liquid patterns fabricated with preprogrammed CPF arrays. **f**, Basic principles of programmable 3D binary liquid patterning. **g**, Using 3D alternating CPFs to sequentially capture red-dyed gellan gum solution and blue-dyed water, the 3D binary liquid pattern with alternating red and blue pixels was prepared. **h**, Vitamins B_2 and B_{12} were patterned in predesigned CPFs consisting of a truncated icosahedron frame and 34 cubic frames, where vitamin B_{12} is encapsulated in the truncated icosahedron frame and vitamin B_2 is captured in the cubic frames. **i**, Demonstration of the release process of vitamins B_2 and B_{12} in water. **j**, Corresponding release profiles of vitamins B_2 and B_{12} (data are presented as mean ± s.d. of $n = 3$ replicates). In **c**–**e** and **g**–**i**, the scale bars are 3 mm.

Combined with interfacial polymerization, multiliquid patterning can readily be achieved and enable multimaterial manufacturing. Three-dimensional patterning of two different photopolymers was achieved with CPFs as shown in Extended Data Fig. 6, where a solid structure consisting of three kinds of photopolymer was obtained via photopolymerization. In addition, just using captures to capture different photopolymers, combined with photopolymerization, a variety of multimaterial manufacturing is implemented (Extended Data

Fig. 7). As a simple and straightforward multimaterial manufacturing method, CPFs with switchable functions of capturing and releasing may provide a facile route to fabricate complex multifunctional structures composed of multimaterials.

Applications in interfacial processes

Switchable liquid capture and release enables a versatile interfacial processing platform as shown in Fig. 4a. To increase the fluid interfacial area, the reactant liquid is first dispersed into a 3D liquid array using the CPF array, under the condition that the size of the PF is smaller than the capillary length as well as the distance between adjacent frames[24,25] (Supplementary Discussion 4). After the interfacial processes, by converting the capture into release, the dispersed liquid can be completely recovered to facilitate the concentration, purification and detection of the products. This platform is generally applicable to both gas–liquid and liquid–liquid interface processes.

We first explored liquid–liquid interfacial processes (that is, diffusion and mixing) with the application of switchable sampling and releasing. Owing to their simplicity in absorbing liquids, sampling tools such as cotton swabs and flocking swabs are extensively used in diagnosis, dressing and clinical medicine. However, these tools suffer from sample residues during their sample release, greatly reducing their detection accuracy and leading to material waste. CPFs can potentially address this challenge because their frame structure renders free liquid–liquid interfaces for the full release of samples. Moreover, the release process will not cause shear-induced sample rupture associated with traditional pipette tools[26], an issue in processing objects such as cells, enzymes and proteins. The quantitative sampling and release experiments of insulin (Fig. 4b) and vitamin B_{12} solutions (Supplementary Fig. 9a) are performed with the CPF, cotton swab and flocking swab. Their release curves verify that the CPFs can completely release the sample in a few seconds, but both flocking and cotton swabs can only release part of the sample. The improved release capacity of the CPFs was also corroborated by a qualitative dye-release experiment (Supplementary Fig. 9b), showing complete release of dye with the CPF even without applying any stirring, but obvious dye residues associated with the cotton and flocking swabs. Using the influenza virus as an example, we demonstrate the practical utility of CPFs as sampling tools with improved release performance. As shown in Fig. 4c and Supplementary Fig. 9c, when the virus concentration was low (1×10^4 to 5×10^4 plaque-forming units (PFU) ml^{-1}), only the CPFs detected the virus, while both the flocking swab and cotton swab showed false negative results. Besides, compared with cotton swabs, the CPFs exhibited comparable liquid absorption capacity for both hydrophilic and hydrophobic surfaces and can maintain sufficient mechanical strength even under repeated large deformations (Supplementary Video 10). Therefore, as supplementary sampling tools with improved release capacity, CPFs can improve the detection accuracy of bioassays such as coronavirus disease 2019 testing, while reducing the required sample volume.

In addition, the use of interfacial gelation enables the application of CPFs in biomaterial encapsulation. As shown in Fig. 4d and Extended Data Fig. 8, when *an Acetobacterium* solution containing $CaCl_2$ captured in the CPFs contacts with the sodium alginate solution, a semi-permeable hydrogel membrane will be formed to encapsulate the *Acetobacterium* in the CPFs. The microscopic morphology of the semipermeable membrane presents a porous structure with a pore diameter of about 50 nm. Therefore, during a microbial electrosynthesis reaction, the micrometer-scale *Acetobacterium* are confined to the membrane, the gas reactants including H_2 and CO_2 can enter the membrane in time to be replenished, and the acetate product can diffuse out. This is confirmed by the experimental results in Fig. 4e, where the acetate concentration in the reactor continued to increase while the bacteria concentration in the reactor (optical density measured at 600 nm, OD_{600}) was almost constant, indicating that the bacteria were successfully encapsulated in the CPFs. This can facilitate the separation of bacteria and reaction products, simplify the microbial reaction process and enhance the utilization rate of bacteria. In addition, CPFs can also potentially be used to encapsulate other biological materials such as algae and cells.

Next, we investigated gas–liquid interfacial processes including evaporation, adsorption, diffusion and reaction, using an evaporative humidifier and CO_2 capture as examples. Figure 4f illustrates the evaporative humidifier. By introducing dry air (humidity 10% at 21 °C) into a sealed chamber equipped with a water-captured CPF array, the humidified air can be output as the droplets evaporate (Supplementary Fig. 10). The output air humidity can be adjusted from 40% to 80% at 21 °C depending on the airflow speed. Notably, experiments have shown that directly introducing dry air into water confined in the bottle cannot effectively humidify the air due to the limited gas–liquid contact area/time. To further demonstrate the practicability of CPF-based evaporative humidifiers, we prepared a commercial-scale humidifier prototype as shown in Extended Data Fig. 9. The experimental results show that the humidification volume is 760 ml h^{-1}, humidification efficiency is 12.6 ml h^{-1} W^{-1} and humidified air output is about 2,000 m^3 h^{-1}. Compared with commercial paper-based evaporative humidifiers, our CPFs-based humidifiers have a higher water storage capacity and require less water flow, making them potentially more energy efficient. Furthermore, unlike paper-based materials, CPFs can be easily customized through additive manufacturing, and the structure is reusable. In addition, compared with the continuous liquid formed by the reported 3D capillary structure[27], the CPFs allow large-scale 3D liquid dispersion to form a larger surface area with less resistance to airflow, leading to greater airflow flux and higher humidification efficiency. An ideal CO_2 cycle process performed with our platform is exhibited in Fig. 4g, which includes carbon capture and storage and CO_2 reutilization[28]. Na_2CO_3 solution dissolved with thymol blue serves as the absorbent. The absorption efficiency of the same amount of absorbent in the bottle and the CPF array are compared. During the experiment, CO_2 is directly introduced into the absorbent in the bottle, and the absorbent in the array absorbs the overflowed CO_2. Absorbents in the array exhibit noticeable color changes earlier and faster, showing higher capture efficiency (Extended Data Fig. 10). After the absorption, the absorbent in the array can be fully recovered by a soap film array for CO_2 storage. Subsequently, heating the recovered absorbent can release CO_2 for applications such as enhanced oil and gas recovery, winemaking, artificial rainfall and so on[29], while both the array and absorbent can be reused for carbon capture and storage. Altering the liquid composition and gas environment, the platform is also applicable to other gas–liquid interfacial processes, such as the toxicity of e-cigarettes to lung tissue cells, harmful gas absorption and environmental monitoring.

Discussion

In summary, we have shown the liquid-steering dictation of the liquid continuity between the frames with CPFs, thereby offering the programmable, switchable capturing and releasing of liquids. This enables a variety of 3D liquid manipulations, including reversible capturing and releasing, programmable 3D patterning and large-scale 3D multiliquid manipulation, simply through a small change in the frame connections without involving complicated equipment and cumbersome fabrication processes. The CPFs offer a versatile fluidic platform, where the captured liquids are omnipotent carriers of myriad target materials, and the structured liquid interfaces can facilitate or enhance diverse interfacial processes. A straightforward combination between different CPFs, captured liquids and interfacial processes will readily expand their applications to multiple disciplines. First, changing the base material or surface chemistry of the frames could inspire and enable some unique applications. For instance, frames printed from biocompatible materials such as stainless steel, PLA or PU can be applied to in vivo or in vitro biological applications. Frames made of 'smart' materials can endow CPFs with specific responses to external stimuli (including

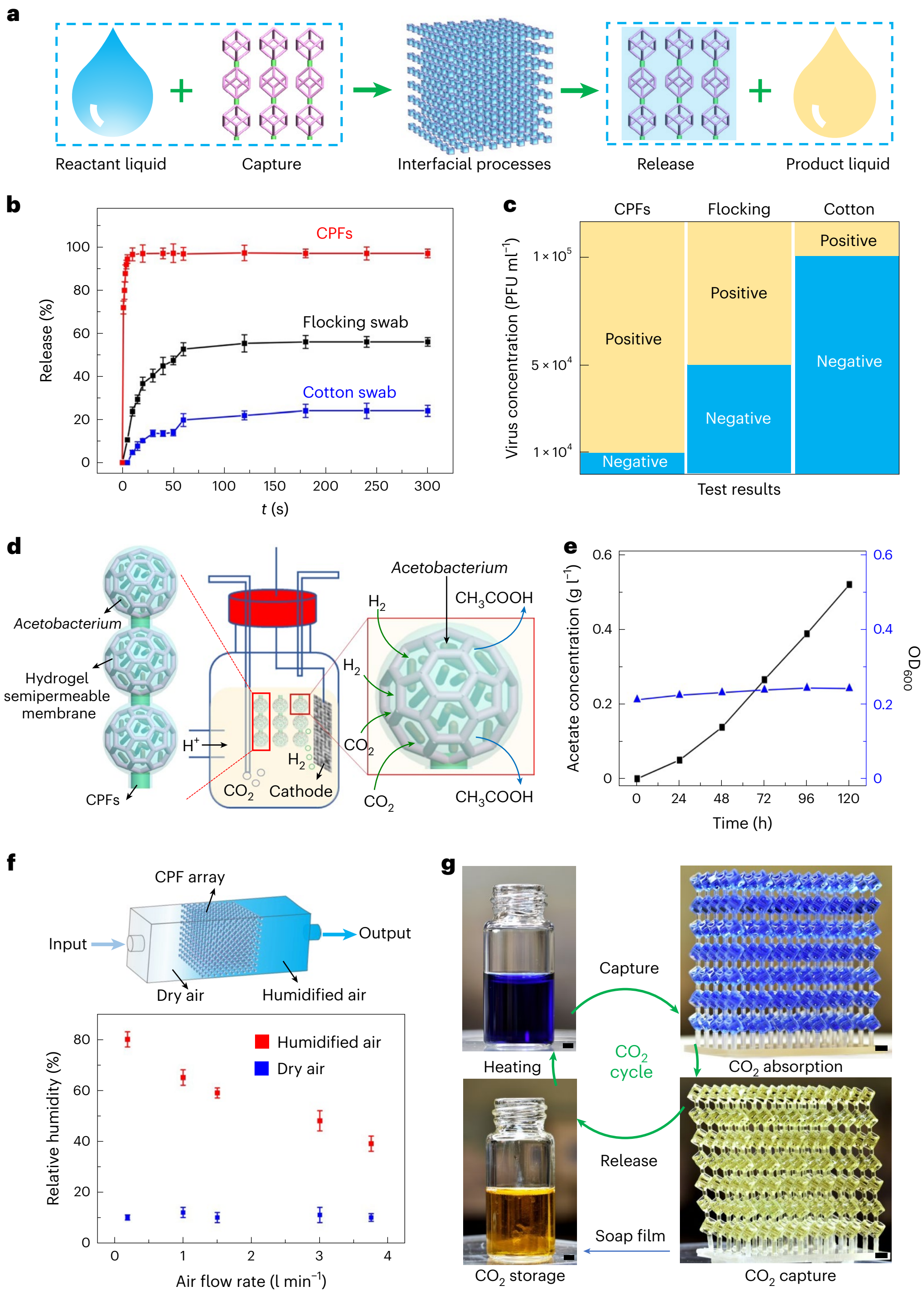

Fig. 4 | Applications in interfacial processes. **a**, Versatile interfacial process platform based on CPFs. The reactant is first dispersed into a liquid array using capturers. After the interfacial processes, by contacting the capturers with liquid films, the dispersed liquid can be completely recovered to facilitate product processing. **b**, Reversible sampling and release demonstration. The insulin release curve of the CPFs, cotton swab and flocking swab in water (data are presented as mean ± s.d. of $n = 3$ replicates). **c**, Influenza virus sampling and detection results of the CPFs, cotton swab and flocking swab. **d**, Schematic illustration of bacterial encapsulation. After encapsulation by interfacial gelation, the *Acetobacterium* are confined in the semi-permeable membrane, the reactants can enter the membrane timely to be replenished and the products can diffuse out. **e**, Concentrations of acetate and suspended bacteria in solution versus time. **f**, Evaporative humidifier demonstration. The dry air passes through the water-captured CPF array, and the humidified air is output as the water droplets evaporate. The output humidity can be adjusted by the airflow rate (data are presented as mean ± s.d. of $n = 3$ replicates). **g**, Demonstration of CO_2 capture. The CPF array first disperses the absorbent, and after absorbing CO_2, the droplets are recovered by the soap film array for CO_2 storage. Subsequently, heating the recovered liquid can release CO_2 on demand. Scale bars, 3 mm.

acoustic, optical, electrical, thermal and magnetic) to encode and derive biomimetic functions[30]. Imparting different wettability to the frames through surface modification would enable 3D patterning of hybrid fluids of gases and liquids to help unravel complex biological multifluid interface conundrums[31]. Integrating frames with different geometries and using their array to achieve 3D multiliquid patterning will offer opportunities to mimic the multicomponent hierarchical structures of tissues or organs[17]. Moreover, the dimensions of the frame structure can be extended across scales, from the millimeter to meter scale, to meet different requirements in applications. In terms of the captured liquid composition, the CPFs are compatible with a wide variety of chemicals and biomaterials ranging from aqueous solutions to biological fluids, hydrogels, organic solvents, polymer solutions and silicone oils, rendering easy routes to explore cell biology, tissue engineering[19], drug screening[32], chemical reactions[16] and multimaterial integration[20]. Combined with different interfacial reactions, various membrane structures can be created on the CPFs, which can be used for controllable drug release[10], artificial cell membranes[33] and biomaterial encapsulation[34]. Therefore, the switchable capturers and releasers offer numerous possibilities for 3D fluidic manipulation, interfacial processes and biotechnological innovation.

Methods

Fabrication and manipulation of the CPFs

The CPFs are printed by the Asiga Freeform Pico 2 printer using the commercial resin PlasCLEAR V2. In Supplementary Fig. 3, the stainless-steel CPFs were printed by a commercial selective laser melting printer, and the PLA and PU CPFs were printed by a commercial fused deposition modeling printer. A homemade lifting system is used for dynamic manipulation. The lifting motion is controlled by a motorized precise translation stage that can drive the printed CPFs to move in a prescribed path, and the moving direction and speed can be precisely adjusted.

Liquids preparation for 3D liquid patterning and application

For visualization purposes, the blue liquids in Figs. 1–4 are pure water mixed with blue edible dye in a volume ratio of 100:1. Soap films in Supplementary Fig. 6 are prepared with the soap solution consisting of 50 g dishwashing agent, 30 g sugar and 150 g distilled water and are selectively pierced with a cotton swab to obtain the predesigned patterns (Supplementary Fig. 6c_2–c_4). The red droplets in Fig. 3g and Supplementary Fig. 7 are 0.8 wt.% gellan gum aqueous solution mixed with red edible dye in a volume ratio of 100:1. The green droplets in Supplementary Fig. 7 are 0.1 wt.% gellan gum aqueous solution mixed with green edible dye in a volume ratio of 100:1. For the controlled release demonstration of vitamins B_{12} and B_2 encapsulated in the CPFs, 1 mg ml^{-1} of vitamin B_{12} was dissolved in 1 wt.% $CaCl_2$ aqueous solution (Fig. 3h,i, red liquids) and 0.3 mg ml^{-1} of vitamin B_2 was dissolved in 0.8 wt.% gellan gum aqueous solution (Fig. 3h,i, yellow liquids). To obtain the binary liquid pattern in Fig. 3h, the truncated icosahedron capturer first captured the vitamin B_{12}-dissolved $CaCl_2$ aqueous solution, then the structure was dripped into the 1 wt.% sodium alginate bath near the liquid surface under stirring for 2 min. After being washed with distilled water, the structure was rinsed in $CaCl_2$ aqueous solution for 2 min to stabilize the hydrogel membrane. After the stabilization, the structure was washed twice with distilled water. Subsequently, because the gellan gum solution has a high viscosity and low fluidity at low temperature (40 °C), the releaser has little time to release the liquid, so the viscous gellan gum dissolved with vitamin B_2 was captured. The release profiles of vitamins B_2 and B_{12} shown in Fig. 3i were measured using the Varian Cary 100 Bio UV–vis spectrophotometer. At scheduled time intervals, the amount of released vitamins B_{12} and B_2 were determined from solution absorbance at 361 and 444 nm wavelengths, respectively. For the multimaterial manufacturing experiments (Extended Data Figs. 6 and 7), commercial photopolymers of different colors and properties were applied to exemplify different kinds of material composition. After each photopolymer is captured or injected into the CPFs, it was irradiated under an ultraviolet lamp for 120 s to obtain a fully cured solid structure.

Reversible sampling and release

For quantitative comparison experiments in Fig. 4b and Supplementary Fig. 9a, three connected truncated icosahedral PFs with a of 1.6 mm, four cotton swabs and six flocked swabs, each as a group, were applied to compare their release efficiency. Each of them can absorb an equal amount of liquid (about 0.56 g). Insulin (10 mg ml^{-1}) and vitamin B_{12} (1 mg ml^{-1}) were selected as sample representatives for macromolecular and small-molecule biomaterials, respectively. After sampling, they were released in 10 ml of water and the diffusion-dominated release processes were recorded by the Varian Cary 100 Bio UV–vis spectrophotometer. At scheduled time intervals, the amounts of released vitamin B_{12} and insulin were determined from solution absorbance at 361 and 276 nm wavelengths, respectively. For the qualitative comparison experiments in Supplementary Fig. 9b, the truncated icosahedron PF with a of 1.2 mm was used to compare the dye release efficiency with cotton and flocking swabs. After capturing the same mass (0.1 g) of green dye solution (volume ratio of 10:1), these sampling tools were released in 8 ml water for 1 min, and the release process was recorded.

Sampling and detection of influenza virus at low concentrations

For influenza virus sampling and detection experiments (Fig. 4c and Supplementary Fig. 9c), the H1N1 virus samples with a concentration of 10^7 PFU ml^{-1} were provided by the second medical center, Chinese PLA General Hospital, under the requirements of medical ethics. It was diluted with the phosphate-buffered saline buffer to a series of concentrations of 10^4, 3×10^4, 5×10^4, 7×10^4 and 10^5 PFU ml^{-1}, respectively. The virus samples were measured by the commercial Wondfo Influenza A/B virus Antigen Detection Kit based on the colloidal gold method. First, 20 µl of the diluted virus solution was collected with the CPFs, cotton swab and flocking swab, respectively. After sampling, the sampling tool was soaked in 500 µl of extraction solution, and the sampling tool was stirred and rotated for 10 s to completely mix the sample with the lysate. Subsequently, three drops of the extraction solution were taken and dropped on the sample hole, and the detection result was read after 10 min.

Bacterial encapsulation

The inoculum used in the bacterial encapsulation experiments was an enriched *Acetobacterium*-dominated mixed culture with a concentration of 1 wt.% $CaCl_2$. Before bacterial encapsulation, the CPFs were treated with oxygen plasma for 2 min to obtain a superhydrophilic surface. The bacterial solution containing 1 wt.% $CaCl_2$ was first captured by the CPFs and then immersed in a 1 wt.% sodium alginate solution for 2 min for interfacial gelation to complete bacterial encapsulation. After cleaning the encapsulated structure with distilled water, it was immersed in 1 wt.% $CaCl_2$ solution for 2 min to stabilize the hydrogel membrane. After cleaning the structure with distilled water, it was immersed in the reaction solution for microbial electrosynthesis. For the characterization of the microstructure of semipermeable hydrogel membranes (Extended Data Fig. 8c,d), membranes on the CPFs were treated with critical point drying using K850 Critical Point Dryer with CO_2. Ethanol was used as the solvent during dehydration. The microstructures of the dried membranes were characterized by scanning electron microscopy.

The classical H-type reactor was used for the microbial electrosynthesis reaction (Extended Data Fig. 8a,e). The bacterium-encapsulated capturers were put in the cathode reaction chamber, which was separated from the cathode compartment with a cation exchange membrane. The cathode, anode, catholyte, anolyte and other reaction conditions were the same as in a previous report[35]. Every 24 h, 5 ml of catholyte was sampled for the pH measurement, volatile fatty acid (VFA) analysis and suspended microorganism concentration measurement. After sampling, the same amount of fresh catholyte was injected and the pH of the catholyte was kept at 7 with 1 mol l^{-1} of NaOH solution. The acetate concentration in the solution was obtained by the VFA analysis with gas chromatography. The VFAs in the liquid samples were extracted by diethyl ether first and then analyzed by gas chromatography with a flame ionization detector and a capillary column. Nitrogen was used for the particles gas with a flow rate of 9.4 ml min^{-1}, and the temperature of the injector and the detector was 230 °C. For the suspended microorganism concentration analysis, the optical density of the liquid samples was measured at 600 nm (OD_{600}) using an ultraviolet–visible spectrophotometer. The change in OD_{600} was used as an indicator of whether bacteria escaped out of the capturers.

Evaporative humidifier

Three sealed cubic acrylic boxes (10 cm × 10 cm × 10 cm) were used as gas flow chambers. Each chamber was equipped with a humidity sensor to record the humidity change at 21 °C, and the CPF array capturing 9.6 g of water droplets was placed in the second chamber as an air humidification chamber. The dry air entered the first chamber first and then passed through the second chamber to deliver the humidified air to the third chamber. Using different airflow rates, the stable humidity of the air output from the third chamber was recorded. In addition, we also measured the humidity of the output air after introducing dry air directly into the water (9.6 g) confined in a bottle, as the reference group. To demonstrate the practicality of capturer-based evaporative humidifiers, we printed large-scale CPF arrays (30 cm × 30 cm × 5 cm) and fabricated a commercial-scale humidifier prototype (Extended Data Fig. 9). The working performance of the humidifier was tested in a closed room of 7.0 m × 7.0 m × 3.2 m, and the room temperature was about 14 °C.

CO_2 absorption

A sealed cubic acrylic box of size 10 cm × 10 cm × 10 cm was used to carry out CO_2(g) absorption experiments. The 5 g ml^{-1} sodium carbonate (Na_2CO_3) aqueous solution dissolved with 0.005 wt.% thymol blue was used as the liquid absorbent. The designed CPF array can capture 6 g of absorbent, so a glass bottle loaded with 6 g of absorbent was also placed in the sealed box as a reference comparison. CO_2(g) was first introduced into the absorbent in the bottle, and the absorbent captured in the array absorbed the overflowing CO_2. Every 5 min, a camera was used to record the color change of the absorbent in the bottle and the array. After 30 min, all the droplets in the array completely turned yellow, the experiment was terminated and the absorbent in the array was recovered with a soap film array.

Numerical simulations

The finite element modeling of the capillary rise in lifting tubes of uniform and nonuniform cross-section (Supplementary Video 3) was performed using COMSOL Multiphysics 5.6. The two-phase flow and phase-field modules were applied, and 2D models were used for simplification. The contact angle between the tube and the liquid (pure water) was 60°. The lifting of the tube was simulated with the moving mesh at a speed of 1 mm s^{-1}. The uniform tube had an inner diameter of 2 mm. The minimum inner diameter of the nonuniform cross-section tube was 0.7 mm, and its capillary rise height varied as the tube was lifted. The finite element modeling simulation of the multisubstance diffusion in Extended Data Fig. 5 was performed using the module of the transport of diluted species in COMSOL Multiphysics 5.6. Substances A and B are assumed to have the same diffusion coefficient of 10^{-7} m^2 s^{-1} and the same initial concentration of 0.1 mol l^{-1}. The diffusion medium was water, and the diffusion time was 300 s.

The lifting process of the CPFs from water into air was simulated by a pseudopotential two-phase lattice Boltzmann model[36,37]. The computational domain was 9 mm × 9 mm × 27 mm. The cube CPFs had a side length of 3 mm and a diameter of 400 μm. The vertical connection between the cubes was 1 mm with a diameter of 800 μm, while the inclined connection was 6.2 mm with a diameter of 400 μm. The CPFs were first immersed in water with a constant contact angle of 60°. Instead of moving the CPFs upward as in the experiment, we let the water flow downward instead (1.7 mm s^{-1}). The dominant nondimensional numbers, that is, capillary number (Ca, 4.6×10^{-4}) and Bond number (Bo, 2.2) were kept similar as in the experiment, to physically model the interactions between capillary, viscous and gravitational forces. When studying the influence of the contact angle of the frame on h_{max} of the releasers, only the corresponding contact angle varied, and other simulation parameters remained unchanged. For capturers, the water was always trapped in the cubes owing to the large capillary force. For releasers, the water was first trapped in the cubes, and then it is released due to continuous gravitational flow.

Data availability

All data are available within the paper and its Supplementary Information.

References

1. Li, W., Tang, X. & Wang, L. Photopyroelectric microfluidics. *Sci. Adv.* **6**, eabc1693 (2020).
2. Tang, X. et al. Mechano-regulated surface for manipulating liquid droplets. *Nat. Commun.* **8**, 14831 (2017).
3. Zhu, P. & Wang, L. Microfluidics-enabled soft manufacture of materials with tailorable wettability. *Chem. Rev.* **122**, 7010–7060 (2022).
4. Feng, S. et al. Three-dimensional capillary ratchet-induced liquid directional steering. *Science* **373**, 1344–1348 (2021).
5. Tang, X., Li, W. & Wang, L. Furcated droplet motility on crystalline surfaces. *Nat. Nanotechnol.* **16**, 1106–1112 (2021).
6. Han, X. et al. Slippery damper of an overlay for arresting and manipulating droplets on nonwetting surfaces. *Nat. Commun.* **12**, 3154 (2021).
7. Tang, X. et al. Design of multi-scale textured surfaces for unconventional liquid harnessing. *Mater. Today* **43**, 62–83 (2021).
8. Aussillous, P. & Quéré, D. Liquid marbles. *Nature* **411**, 924–927 (2001).
9. Borrelle, S. B. et al. Predicted growth in plastic waste exceeds efforts to mitigate plastic pollution. *Science* **369**, 1515–1518 (2020).
10. Zhang, Y. et al. Magnetic-actuated 'capillary container' for versatile three-dimensional fluid interface manipulation. *Sci. Adv.* **7**, eabi7498 (2021).
11. De Gennes, P.-G., Brochard-Wyart, F. & Quéré, D. *Capillarity and Wetting Phenomena: Drops, Bubbles, Pearls, Waves*. Vol. 315 (Springer, 2004).
12. Young, D. F., Munson, B. R., Okiishi, T. H. & Huebsch, W. W. *A Brief Introduction to Fluid Mechanics* (John Wiley & Sons, 2010).
13. Vrij, A. Possible mechanism for the spontaneous rupture of thin, free liquid films. *Discuss. Faraday Soc.* **42**, 23–33 (1966).
14. Vrij, A. & Overbeek, J. T. G. Rupture of thin liquid films due to spontaneous fluctuations in thickness. *J. Am. Chem. Soc.* **90**, 3074–3078 (1968).
15. Levskaya, A., Weiner, O. D., Lim, W. A. & Voigt, C. A. Spatiotemporal control of cell signalling using a light-switchable protein interaction. *Nature* **461**, 997–1001 (2009).
16. Aubert, S., Bezagu, M., Spivey, A. C. & Arseniyadis, S. Spatial and temporal control of chemical processes. *Nat. Rev. Chem.* **3**, 706–722 (2019).
17. Primo, G. A. & Mata, A. 3D patterning within hydrogels for the recreation of functional biological environments. *Adv. Funct. Mater.* **31**, 2009574 (2021).
18. Krishna Kumar, R. et al. Droplet printing reveals the importance of micron-scale structure for bacterial ecology. *Nat. Commun.* **12**, 857 (2021).
19. Hua, D. et al. Concentration gradients in material sciences: methods to design and biomedical applications. *Adv. Funct. Mater.* **31**, 2009005 (2021).

20. Lee, B. et al. 3D micromesh-based hybrid bioprinting: multidimensional liquid patterning for 3D microtissue engineering. *NPG Asia Mater.* **14**, 1–10 (2022).
21. Shin, Y. et al. Microfluidic assay for simultaneous culture of multiple cell types on surfaces or within hydrogels. *Nat. Protoc.* **7**, 1247–1259 (2012).
22. Kim, H. J., Boedicker, J. Q., Choi, J. W. & Ismagilov, R. F. Defined spatial structure stabilizes a synthetic multispecies bacterial community. *Proc. Natl Acad. Sci. USA* **105**, 18188–18193 (2008).
23. deMello, A. J. Control and detection of chemical reactions in microfluidic systems. *Nature* **442**, 394–402 (2006).
24. Kang, M. et al. Capillarity guided patterning of microliquids. *Small* **11**, 2789–2797 (2015).
25. Huang, Z. et al. A general approach for fluid patterning and application in fabricating microdevices. *Adv. Mater.* **30**, 1802172 (2018).
26. Dunne, P. et al. Liquid flow and control without solid walls. *Nature* **581**, 58–62 (2020).
27. Dudukovic, N. A. et al. Cellular fluidics. *Nature* **595**, 58–65 (2021).
28. E. Boot-Handford, M. et al. Carbon capture and storage update. *Energy Environ. Sci.* **7**, 130–189 (2014).
29. Koytsoumpa, E. I., Bergins, C. & Kakaras, E. The CO_2 economy: review of CO_2 capture and reuse technologies. *J. Supercrit. Fluids* **132**, 3–16 (2018).
30. Roy, D., Cambre, J. N. & Sumerlin, B. S. Future perspectives and recent advances in stimuli-responsive materials. *Prog. Polym. Sci.* **35**, 278–301 (2010).
31. Grigoryan, B. et al. Multivascular networks and functional intravascular topologies within biocompatible hydrogels. *Science* **364**, 458–464 (2019).
32. Feng, W., Ueda, E. & Levkin, P. A. Droplet microarrays: from surface patterning to high-throughput applications. *Adv. Mater.* **30**, 1706111 (2018).
33. Yasuga, H. et al. Fluid interfacial energy drives the emergence of three-dimensional periodic structures in micropillar scaffolds. *Nat. Phys.* **17**, 794–800 (2021).
34. Orive, G. et al. Cell encapsulation: promise and progress. *Nat. Med.* **9**, 104–107 (2003).
35. Xue, X., Liu, Z., Cai, W., Cui, K. & Guo, K. Porous polyurethane particles enhanced the acetate production of a hydrogen-mediated microbial electrosynthesis reactor. *Bioresour. Technol. Rep.* **18**, 101073 (2022).
36. Qin, F., Mazloomi Moqaddam, A., Kang, Q., Derome, D. & Carmeliet, J. Entropic multiple-relaxation-time multirange pseudopotential lattice Boltzmann model for two-phase flow. *Phys. Fluids* **30**, 032104 (2018).
37. Qin, F. et al. Study of non-isothermal liquid evaporation in synthetic micro-pore structures with hybrid lattice Boltzmann model. *J. Fluid Mech.* **866**, 33–60 (2019).

Acknowledgements

This work was supported by the Research Grants Council of Hong Kong with grants GRF 17213823 (L.W.), GRF17205421 (L.W.), GRF17204420 (L.W.), Shenzhen Science and Technology Program with grant JCYJ20210324115412035 (J.Y.) and the high-performance computational resources from Swiss National Supercomputing Centre with grant CSCS s1081 (F.Q. and J.C.).

Author contributions

Y.Z., Z.H., J.Y. and L.W. conceived and designed this work. Y.Z., Z.H., H.W., K.C. and K.G. performed the experiments. Y.Z., Z.H. and L.W. analyzed the data and isolated the mechanisms, Z.H., Z.C., F.Q., J.X. and X.C. conducted the numerical simulations. Y.Z., Z.H., L.W., F.Q., J.Y., J.C., J.W. and Y.S. wrote and revised the paper.

Competing interests

The authors declare no competing interests.

Additional information

Extended data is available for this paper at https://doi.org/10.1038/s44286-024-00090-w.

Supplementary information The online version contains supplementary material available at https://doi.org/10.1038/s44286-024-00090-w.

Correspondence and requests for materials should be addressed to Zhandong Huang, Jun Yang or Liqiu Wang.

Peer review information *Nature Chemical Engineering* thanks David Juncker and Sungyon Lee for their contribution to the peer review of this work.

Reprints and permissions information is available at www.nature.com/reprints.

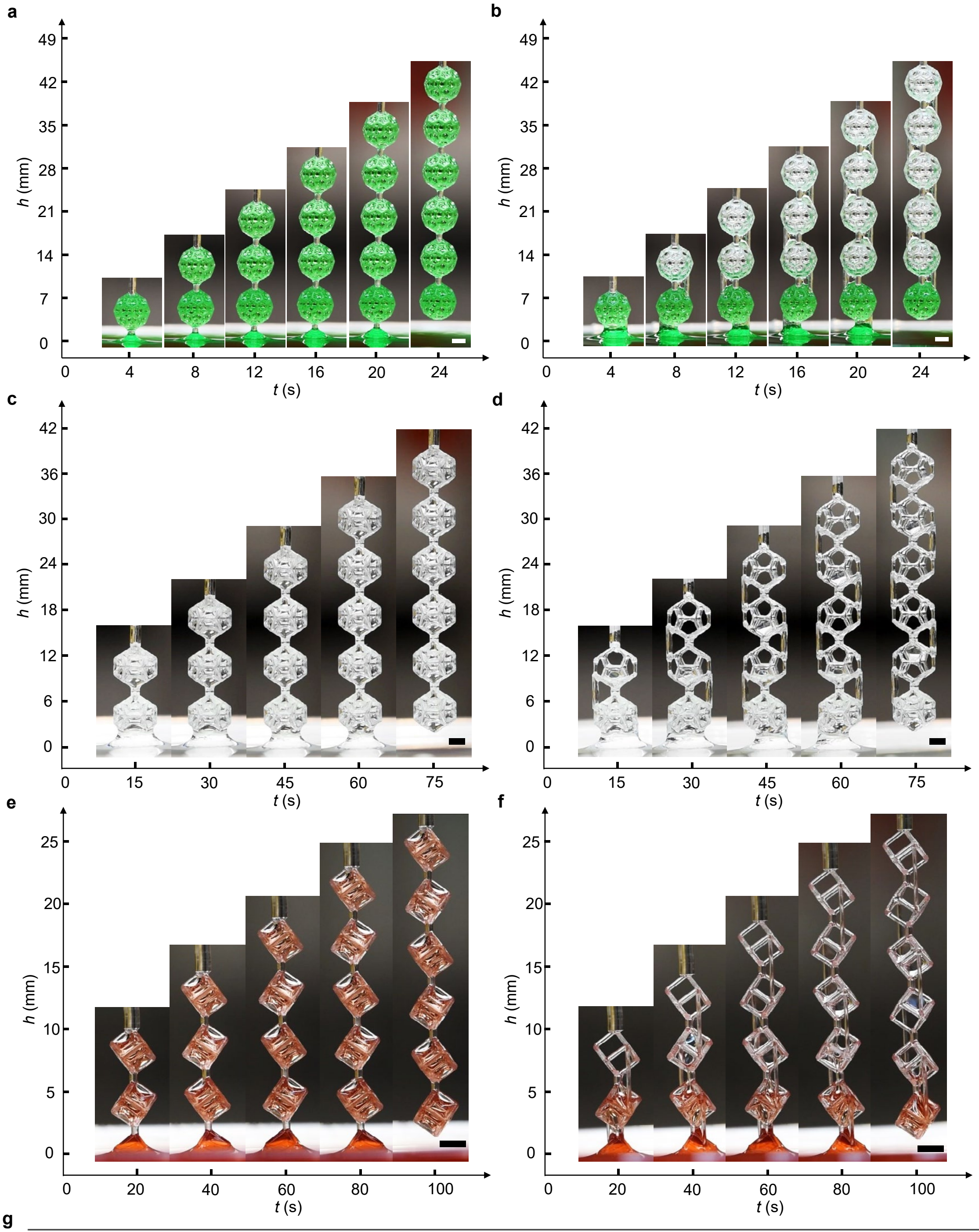

g

Liquid type	Surface tension (mN·m^{-1})	Viscosity (10^{-3}Pa·s)	Density (g·cm^{-3})	Capillary length (mm)	Boiling point (° C)	Vapor pressure at 20.0 ° C (mmHg)
Aqueous solution	72.75	0.8984	1	2.7	100° C	17.54
Ethylene glycol	48.4	16.1	1.113	2.1	197 °C	0.06
Photopolymer resins	27	400	1.184	1.5	280 °C	–
Silicone oil	20.8	20	0.95	1.5	>140 °C	5
Ethanol	22.0	1.07	0.787	1.7	78 °C	44
Acetone	23.3	0.31	0.786	1.7	56.05°C	185.5

Extended Data Fig. 1 | Universality of CPFs in different liquids. By designing the size of the PFs within the capillary length of ethylene glycol (**a**, **b**), photopolymer resin (**c**, **d**), and silicone oil (**e**, **f**), when the CPFs are slowly lifted out of the corresponding liquids, the capturers capture the liquids (**a**, **c**, **e**), while the releasers release the liquids (**b**, **d**, **f**). **g**, Table of physical parameters of different liquids. To clearly distinguish the three liquids, ethylene glycol is dyed green with edible dye, and silicone oil is dyed red with Sudan III. Scale bars, 2 mm.

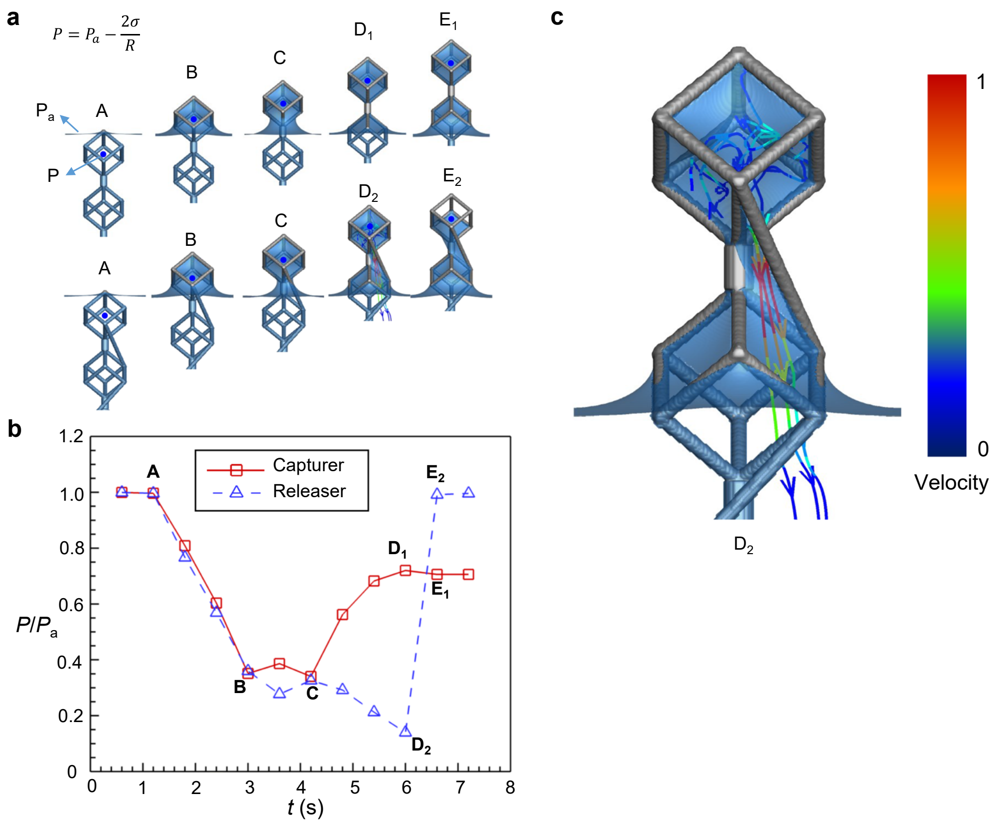

Extended Data Fig. 2 | 3D numerical simulations of the lifting process of the CPFs. a, Typical liquid morphology in the CPFs: D_2 represents the case that the liquid height is at its maximum; E_2 represents the case of the liquid rupture in the releaser. P_a is ambient air pressure. The pressure P at the center of the frame (blue dots in the figure) is used to represent the liquid pressure in the capturer and releaser. $P = P_a - 2\sigma/R$ from the Laplace equation, where R is the curvature radius of the gas-liquid interface in the frame and σ is the surface tension of the liquid. **b**, Evolution of P/P_a. From A to B, as the CPF rises, both R and P decrease in capturer and releaser. From B to C, R changes differently as the single-rod or double-rod connection crosses the gas-liquid interface, and P fluctuates accordingly. After point C, P changes differently in the capturer and releaser. For the capture, the liquid in the frame is separated from the bulk liquid below, and the liquid weight in the frame is independent of the rising height, so P stops decreasing. After the liquid is split, the gas-liquid interface rebounds to increase R, and P also increases until reaching a new equilibrium state (point E_1), where P is slightly smaller than P_a. For the releaser, because the liquid film between the double rods connects the liquid in the frame and the bulk liquid below, the liquid weight in the frame continues to increase with the rising height, and R continues to decrease, P also decreases until the liquid height reaches its maximum, Case D_2. After this critical state, the liquid ruptures in the frame, air fills the frame (E_2), and P becomes P_a. **c**, The flow velocity in the releaser at D_2. During the lifting process, the releaser continuously releases the liquid into the bulk liquid below. The liquid film formed between the double rod connection has a larger flow velocity and can be regarded as a narrow release channel.

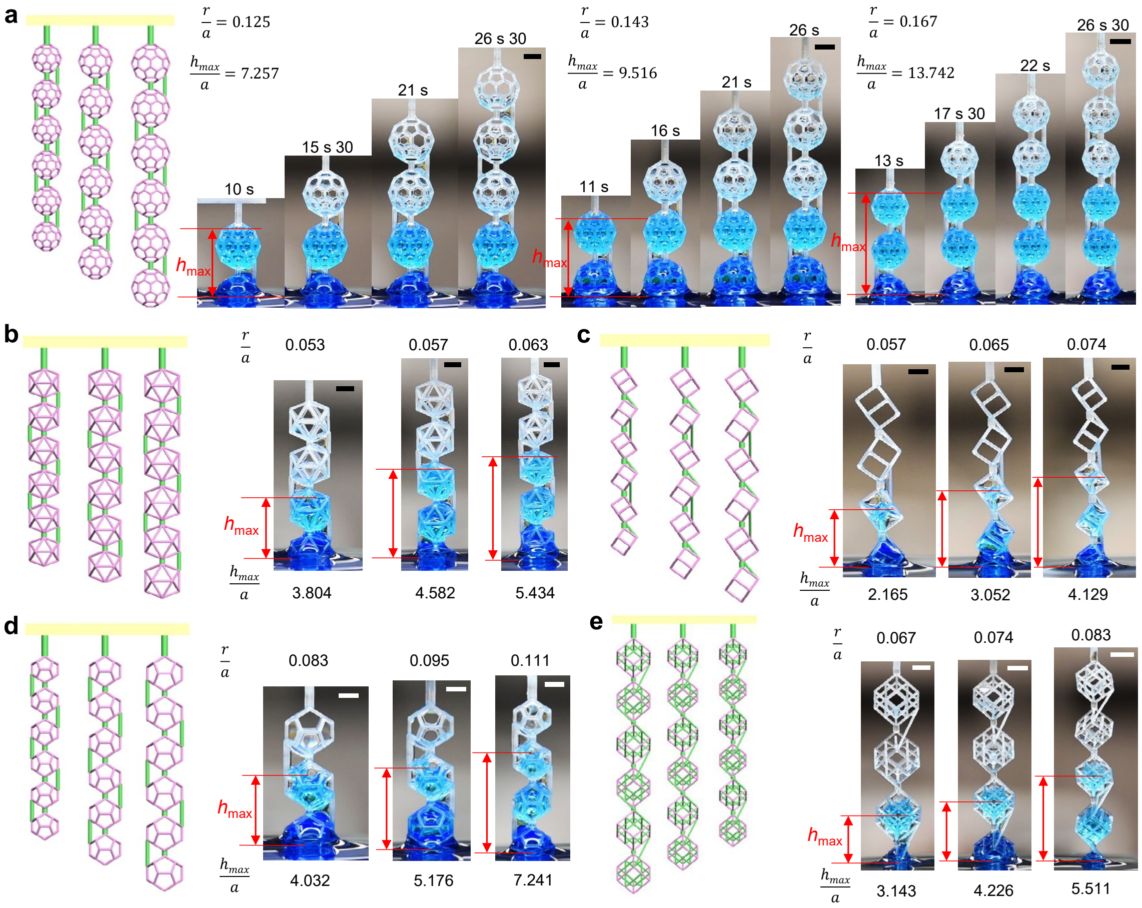

Extended Data Fig. 3 | Experimentally measured data of $\frac{h_{max}}{a}$ for releasers with different geometry and size parameter $\frac{r}{a}$. Releasers with different geometries include truncated icosahedrons (**a**) icosahedrons (**b**) cubes (**c**) dodecahedrons (**d**) and cubes with crossbars on each face (**e**). For the releasers with the same geometry, their $\frac{h_{max}}{a}$ increases as $\frac{r}{a}$ increases.

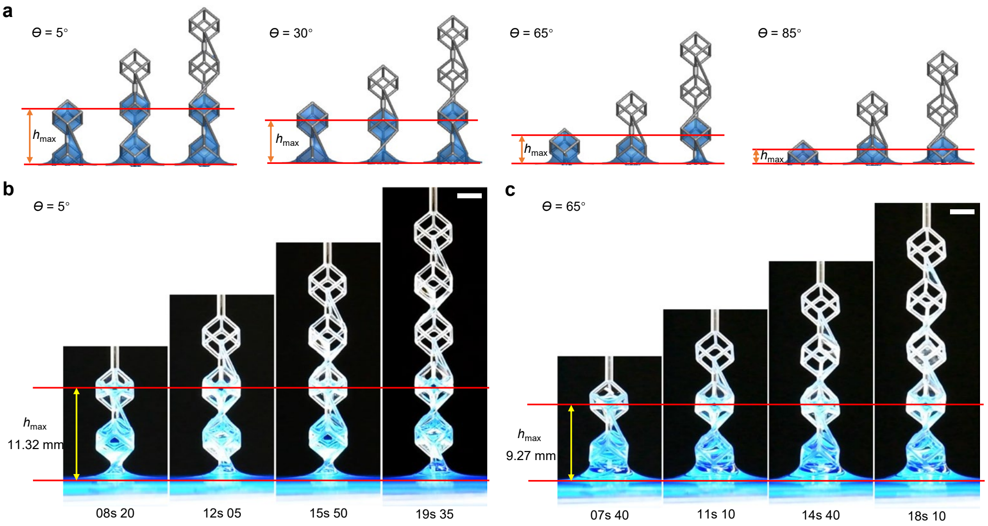

Extended Data Fig. 4 | Influence of frame wettability on h_{max}. **a**, Simulation results of the influence of frame surface contact angle (θ) on h_{max}. **b**, The experimentally measured h_{max} of the cubic releaser with θ of 5°. **c**, The experimentally measured h_{max} of the cubic releaser with θ of 65°. Scale bars, 3 mm. They suggest that h_{max} gradually decreases with the increase of θ.

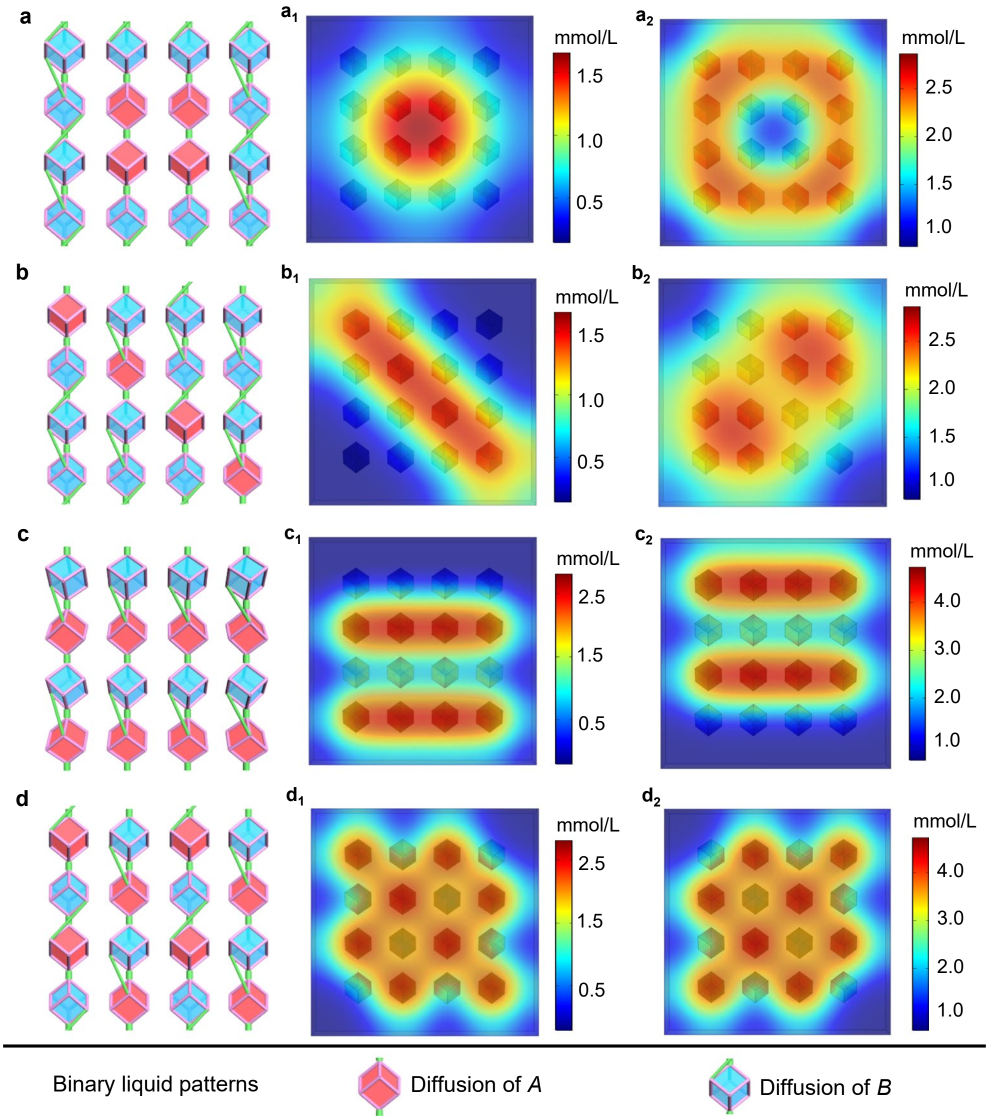

Extended Data Fig. 5 | 3D spatial concentration gradient control of two substances based on 3D binary liquid patterning. (**a**-**d**), Representative binary liquid patterns of two liquids containing different solutes, which can be achieved in experiments using the methods in Fig. 3. To clearly distinguish the two liquids, they are shown in red and blue, where the red liquid contains substance A and the blue liquid contains substance *B*. (**a_1**-**d_1**) Spatial concentration distribution of substance A in the corresponding binary liquid patterns in **a**-**d** after 300 s diffusion in water. (**a_2**-**d_2**) Spatial concentration distribution of substance *B* in the corresponding binary liquid patterns in **a**-**d** after 300 s diffusion in water. The simulation results show that the temporal and spatial concentration distributions of multiple substances can be well controlled using 3D binary liquid patterning. The cubic frame unit has a side length of 3 mm and a rod diameter of 400 μm.

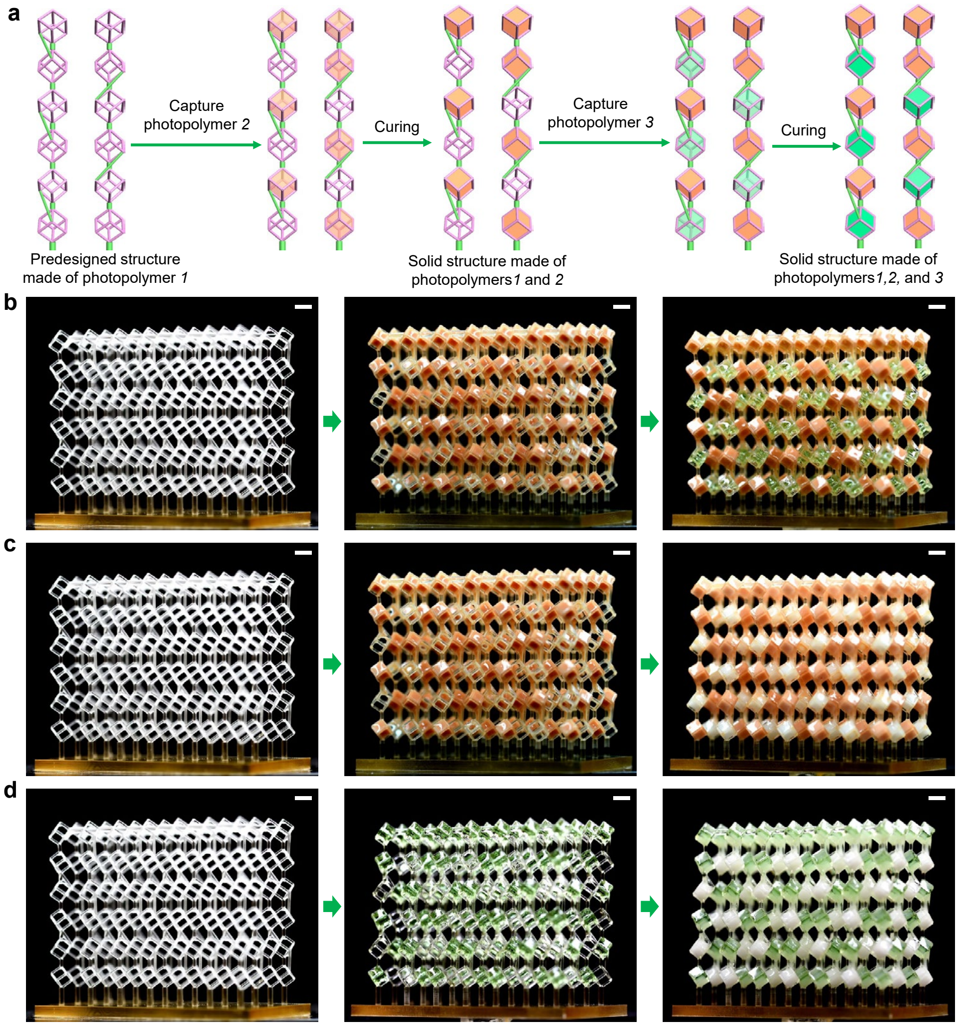

Extended Data Fig. 6 | Multi-material fabrication with CPFs via interfacial polymerization. a, Schematic illustration of multi-material fabrication using CPFs. The capturers composed of photopolymer *1* capture photopolymer *2* first, and forms a solid structure composed of photopolymers *1* and *2* after photocuring. Subsequently, the release-blocked releasers capture photopolymer *3*, forming a solid structure composed of photopolymers *1*, *2*, and *3* after photocuring. **b**, Preparation of solid structures made of transparent, red, and green photopolymers. **c**, Preparation of solid structures made of transparent, red, and white photopolymers. **d**, Preparation of solid structures made of transparent, green, and white photopolymers. Scale bars, 3 mm.

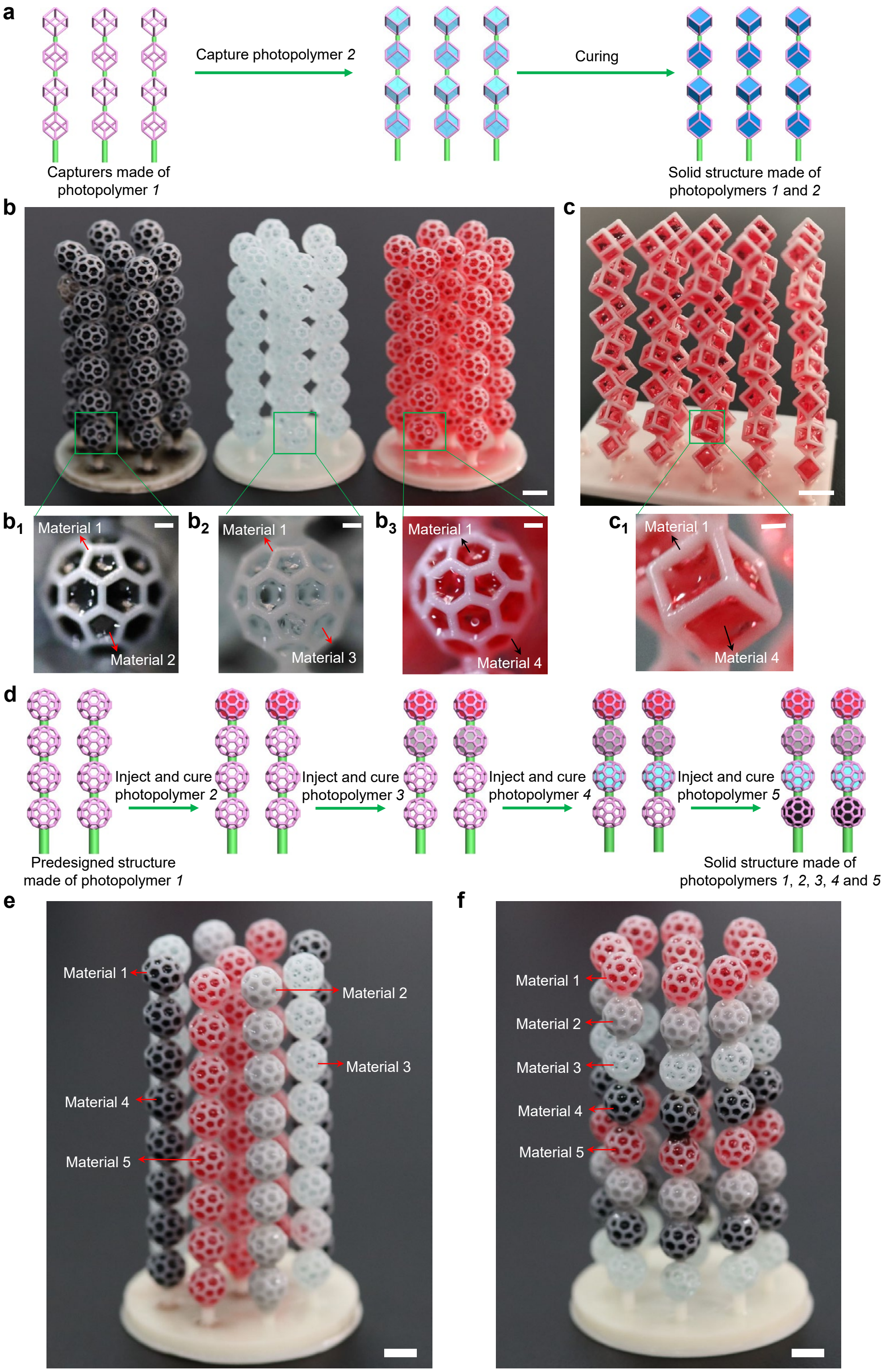

Extended Data Fig. 7 | Multi-material fabrication with capturers via interfacial polymerization. a, Schematic illustration of bi-material fabrication using capturers. The capturers composed of photopolymer *1* capture photopolymer *2* first, and then forms a solid structure composed of photopolymers *1* and *2* after photocuring. (**b**-**c**), Bi-material solid structures fabricated using capturers. Capturers printed with white photopolymer capture black (**b**$_1$), blue (**b**$_2$), and red (**b**$_3$ and **c**$_1$) photopolymer, respectively, to form corresponding bi-material solid structures. **d**, Schematic illustration of multi-material fabrication using capturers. Different types of photopolymers are sequentially injected and cured in capturers at different spatial positions finally forming the expected multi-material solid structure. (**e**-**f**), Multi-material solid structure prepared by capturers. In **b**, **c**, **e**, and **f**, the scale bars are 5 mm. In **b**$_1$-**b**$_3$ and **c**$_1$, the scale bars are 1 mm.

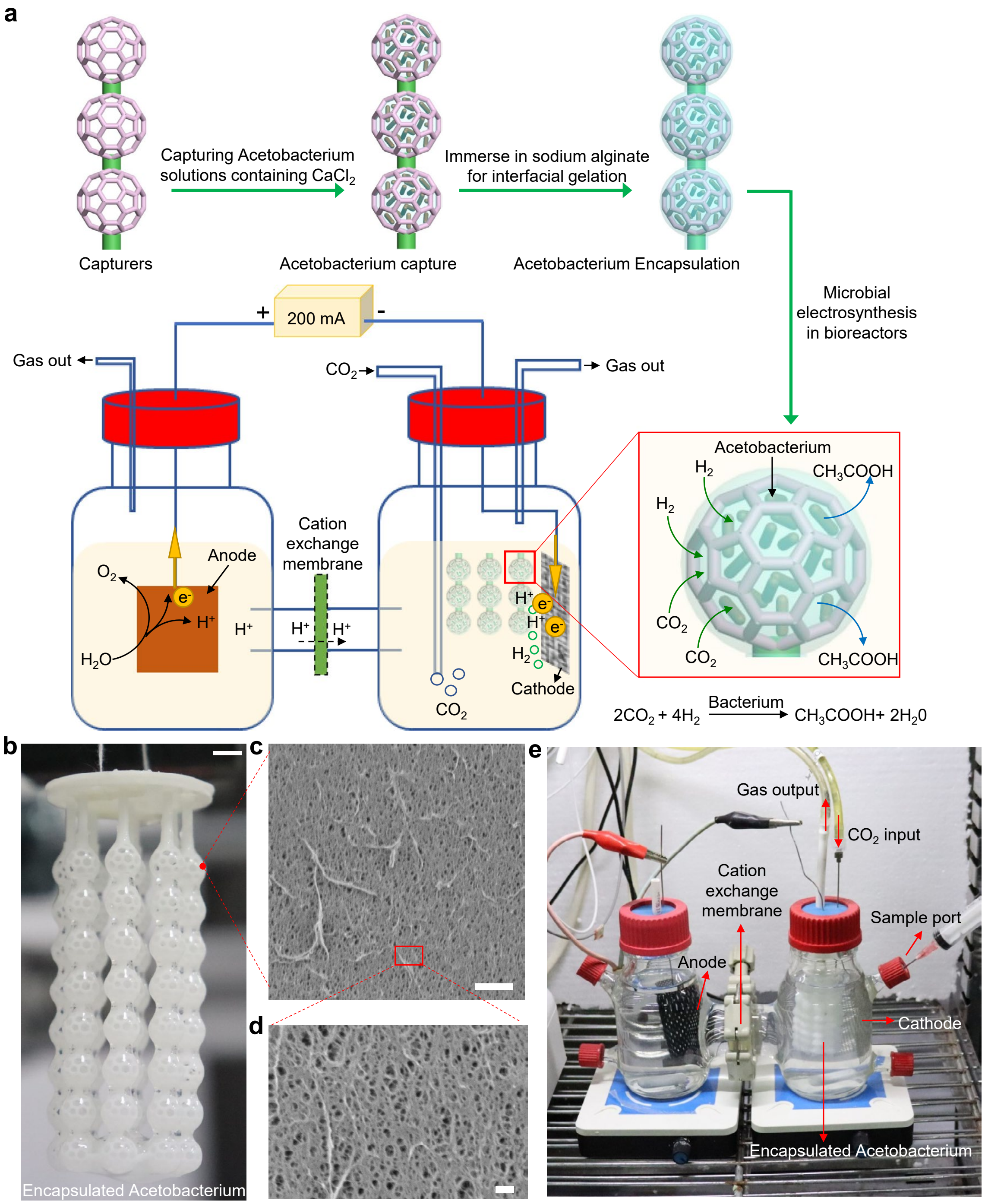

Extended Data Fig. 8 | Bacterial encapsulation applications for separation of microbial electrosynthesis products. a, Schematic illustration of bacterial encapsulation application using CPFs via interfacial gelation. The Acetobacterium solution containing calcium chloride was first captured by CPFs and then immersed in sodium alginate solution for interfacial gelation to form a semipermeable hydrogel membrane to complete Acetobacterium encapsulation. Put the Acetobacterium-encapsulated CPFs into the classical H-type reactor for microbial electrosynthesis reaction, the Acetobacterium are confined in the semi-permeable membrane, the reactants can enter the semi-permeable membrane in time to be replenished, and the reaction products can diffuse out and be separated. **b**, Acetobacterium-encapsulated CPFs with a liquid-core hydrogel-membrane shell structure. Scale bar, 5 mm. (**c**-**d**) Microscopic pore structure of the semipermeable hydrogel membranes. In **c** and **d**, the scale bars are 1 µm and 200 nm, respectively. **e**, Specific experimental setup for bacterial encapsulation applications.

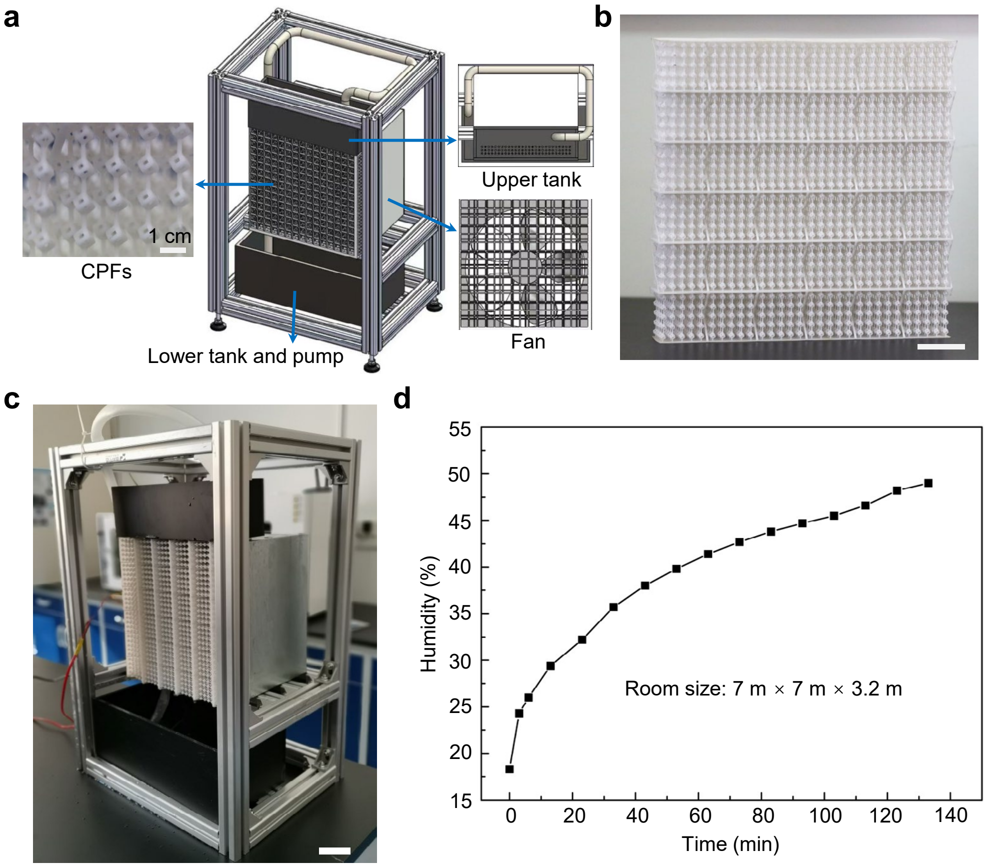

Extended Data Fig. 9 | Commercially-scale evaporative humidifier prototype. **a**, Schematic diagram of the components of the commercially-scale evaporative humidifier prototype. The water pump pumps a continuous flow of water from the lower tank to the porous upper tank to disperse the liquid into the CPF array, thereby increasing the air-liquid interface. The fan behind the CPF array creates a negative pressure, which continuously introduces dry air into the space of the CPF array and outputs humid air. **b**, Photograph of the large-scale CPF arrays. **c**, Photograph of the commercially-scale evaporative humidifier prototype. The CPF array here is rotated by 90 degrees compared to figure **b**, so as to slow down the release of liquid from the upper tank to the lower tank. **d**, The humidity-time curve in a room of 7.0 m×7.0 m×3.2 m. In **b** and **c**, the scale bars are 5 cm.

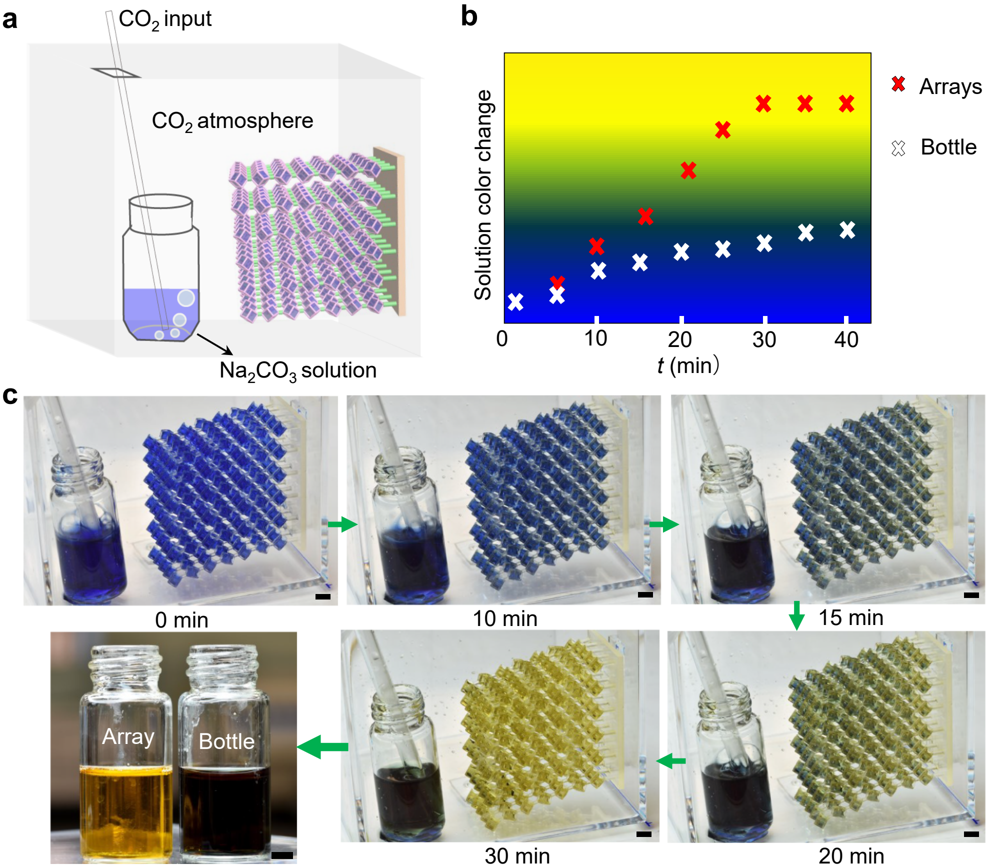

Extended Data Fig. 10 | CO$_2$ absorption experimental setup and color change process. a, Schematic diagram of the experimental setup for CO$_2$ absorption. CO$_2$ is directly introduced into the absorbent in the bottle, and the absorbent in the CPF array absorbs the overflowed CO$_2$. **b**, Color change curves of absorbent in the bottle and array over time. **c**, Photographs of the color change of absorbent in the bottle and array over time. After 30 minutes, the droplets in the array were fully recovered by the soap film array. The solution color in the array was yellower than that of the bottle, indicating a higher CO$_2$ absorption efficiency. Scale bars, 5 mm.